THE GEOLOGICAL SOCIETY OF AMERICA®

Along-strike variation in catchment morphology and cosmogenic denudation rates reveal the pattern and history of footwall uplift, Main Gulf Escarpment, Baja California

Matthew W. Rossi[1,†], Mark C. Quigley[2], John M. Fletcher[3], Kelin X. Whipple[1], J. Jesús Díaz-Torres[4], Christian Seiler[2], L. Keith Fifield[5], and Arjun M. Heimsath[1]

[1]*School of Earth and Space Exploration, Arizona State University, Tempe, Arizona 85281, USA*
[2]*School of Earth Sciences, The University of Melbourne, Melbourne, Victoria 3010, Australia*
[3]*Departamento de Geología, Centro de Investigación Científica y de Educación Superior de Ensenada (CICESE), Ensenada, Baja California 22860, Mexico*
[4]*Tecnología Ambiental, Centro de Investigación y Asistencia en Tecnología y Diseño del Estado de Jalisco (CIATEJ), Guadalajara, Jalisco 44270, Mexico*
[5]*Research School of Physics and Engineering, Australia National University, Canberra, ACT 0200, Australia*

ABSTRACT

Topography is expected to record tectonic, climatic, and rock strength controls on long-term denudation rates in active margins. We test this hypothesis in the Sierra San Pedro Mártir, Mexico—the footwall of the normal-faulted, western margin of the Gulf of California rift system—by relating topographic metrics with ^{10}Be-derived catchment-averaged denudation rates. Denudation rates and topographic metrics record along-strike gradients in rock uplift relative to base level that increase asymmetrically from fault tips to maxima within the northern half of the range. Surface uplift of an Eocene erosional surface and slope-break knickpoints found at increasingly higher elevations in the northern segments of the Sierra San Pedro Mártir fault system suggest that range asymmetry is due to a recent northward acceleration in the rate of rock uplift relative to base level. By characterizing the relationship between channel steepness and cosmogenic denudation rates, we extrapolate millennial-scale denudation rates to million-year time scales and estimate ages for the transient increase in rock uplift rates and the initial onset of normal faulting. We infer that the Sierra San Pedro Mártir fault system initiated during the middle Miocene (ca. 16–14 Ma) in the center of the range and ca. 12–8 Ma near the fault tips. Recent increases in rock uplift rates during the late Pliocene (ca. 3–2 Ma) coincide with lithospheric rupture in the Delfin basins to the east and represent a westward migration of strain from hanging-wall detachments to the Sierra San Pedro Mártir fault system. Age estimates are consistent with independent geologic constraints and show that pairing of carefully selected cosmogenic denudation rates with topographic analysis can be used to extract tectonic signals from topography over million-year time scales.

1. INTRODUCTION

1.1 Motivation and Scope

The Sierra San Pedro Mártir is a prominent section of the Main Gulf Escarpment in Baja California. The Sierra San Pedro Mártir fault system is a steep, large-displacement (breakaway) fault that defines the margin of the relatively unextended rift flank of the Baja California microplate to the west from extension associated with Gulf of California rifting to the east. Despite its regional importance, the tectonic and topographic history of the Sierra San Pedro Mártir remains poorly constrained. In this study, we demonstrate that the uplift history of the normal fault–bounded Sierra San Pedro Mártir is recorded in modern topography and millennial-scale denudation rates. The tectonic forcing of a normal fault block is expected to exhibit a relatively simple along-strike pattern, with maximum rock uplift and maximum subsidence rates in the central portions of the range and total displacement proportional to fault length (Cowie and Scholz, 1992; Dawers et al., 1993). A similar pattern is also expected in mature, multisegment fault systems once individual faults are linked to a through-going structure (Dawers and Anders, 1995). To evaluate this expectation in the Sierra San Pedro Mártir, we used digital elevation model analysis to document systematic along-strike variations in (1) topographic metrics that characterize local relief and (2) a suite of slope-break knickpoints. Furthermore, we show that functional relationships between morphometric data and cosmogenic radionuclide–derived denudation rates (CRN_{DR}) can be used to assess the timing and spatial pattern of normal faulting in the Sierra San Pedro Mártir.

1.2 Approach and Rationale

Topography records the time-integrated history of vertical motions of the crust and the erosional and depositional responses to tectonic and climatic forcing (Anderson and Anderson, 2010). Over the last 15 years, substantial progress has been made in extracting quantitative information about the history of rock uplift relative to base level from topography (e.g., Wobus et al., 2006; Kirby and Whipple, 2012; Whittaker, 2012). In landscapes where mean climate and rock uplift rates relative to base level are

†Present address: Earth Lab, University of Colorado, 4001 Discovery Drive, Boulder, Colorado 80309, USA; matthew.rossi@colorado.edu.

GSA Bulletin; doi: 10.1130/B31373.1; 8 figures; 1 table; Data Repository item 2016296.

steady, geomorphic properties such as channel longitudinal profiles, hillslope gradients, and local relief (measured over 1–2.5 km length scales) evolve toward an equilibrium condition in which denudation rates balance rock uplift rates over the long term (Hack, 1975; Willett and Brandon, 2002). Figure 1 is a cartoon illustrating how these principles can be applied to high-angle, normal-fault settings. In the hanging wall, base level is set by the balance between subsidence and deposition, which are in turn driven by slip on the fault and the load imparted by overlying sediment and water. In the footwall, the morphology of the actively denuding escarpment will evolve toward a balance between denudation rates and rock uplift rates relative to base level. If there is little preexisting topography when footwall uplift initiated, then surface uplift of the stable erosional surface can be used as a structural datum across the fault to infer total rock uplift relative to base level of the footwall since the onset of faulting (for an early example of this approach in a compressional setting, see Spotila et al., 1998).

Growing numbers of studies are showing that spatial patterns in rock uplift relative to base level are well correlated with spatial patterns in topographic metrics for a given lithology and climate (e.g., Snyder et al., 2000; Kirby and Whipple, 2001; Lague and Davy, 2003; Wobus et al., 2003, 2006; Duvall et al., 2004; Harkins et al., 2007; Cyr and Granger, 2008; Whittaker et al., 2008; Olivetti et al., 2012; Ouimet et al., 2009; Cyr et al., 2010; DiBiase et al., 2010; Whittaker, 2012; Godard et al., 2014; Scherler et al., 2014). Furthermore, sustained increases in rock uplift rate relative to base level can be recorded in the topography as a series of slope-break knickpoints in channel profiles, along with associated increases in hillslope gradients and local relief (e.g., Schoenbohm et al., 2004; Clark et al., 2005; Dorsey and Roering, 2006; Wobus et al., 2006; Harkins et al., 2007; Kirby et al., 2007; Miller et al., 2012, 2013; Schildgen et al., 2012; Whittaker and Boulton, 2012; Ellis et al., 2015). Kirby and Whipple (2012) reviewed recent studies that document the transient response of landscape form to increases in rock uplift rate relative to base level and how to best extract this information from the topography. A universal hallmark of the transient response is that longitudinal river profiles contain slope-break knickpoints that are observed as a persistent break in the scaling relationship between drainage area and channel slope (e.g., Wobus et al., 2006; Kirby and Whipple, 2012). A subset of these prior studies showed how the magnitude and timing of changes in rock uplift rates relative to base level can be quantified using the spatial pattern of denudation rates, provided that they are representative of long-term rates of rock uplift relative to base level (see discussion in Kirby and Whipple, 2012).

The widespread use of concentrations of cosmogenic radionuclides (CRN) like ^{10}Be in alluvial sediments to determine catchment-averaged denudation rates over 10^2–10^5 yr, or "millennial," time scales (Bierman and Steig, 1996; Granger et al., 1996) has expanded our knowledge of late Quaternary denudation rates around the world and our ability to test geomorphic hypotheses (von Blanckenburg, 2005; Portenga and Bierman, 2011; Willenbring et al., 2013). For instance, recent studies have found a positive correlation between catchment-averaged hillslope gradient (S_{avg}) and CRN–derived denudation rates (CRN_{DR}) up to a threshold of S_{avg} ~32°–37°, above which S_{avg} becomes invariant with changes in CRN_{DR} (e.g., Binnie et al., 2007; Ouimet et al., 2009; DiBiase et al., 2010; Godard et al., 2014; Scherler et al., 2014). This is consistent with the long-recognized dependence of colluvial erosion on hillslope angle and relief (Ahnert, 1970; Gilbert and Dutton, 1880) until a threshold slope is reached, and then hillslopes respond to further base-level lowering via increased landslide frequency (e.g., Strahler, 1950; Penck, 1953; Schmidt and Montgomery, 1995; Burbank et al., 1996; Hovius et al., 1997; Montgomery and Brandon, 2002; Larsen and Montgomery, 2012). Deep-seated landslides also lead to large spatial and temporal variability in stream sediment CRN concentrations due to the stochastic delivery of CRN-poor material into the catchment network (Niemi et al., 2005; Yanites et al., 2009), particularly where stream sediments have comparably high "background" CRN concentrations (Quigley et al., 2007). Although the possibility has been proposed that CRN concentrations can become "decoupled" from rock uplift rates due to geomorphic inheritance and stochastic sediment delivery to the channels (Densmore et al., 2009) for some normal-fault footwall mountains in the Basin and Range Province, United States, most studies have found consistent relationships among catchment morphology, CRN_{DR}, and longer-term exhumation rates (Safran et al., 2005; Binnie et al., 2007; Harkins et al., 2007; Cyr and Granger, 2008; Ouimet et al., 2009; Cyr et al., 2010; DiBiase et al., 2010; Olivetti et al., 2012; Miller et al., 2013). Nevertheless, how faithfully, and under what conditions, CRN_{DR} can be used to infer exhumation rates over 10^6–10^7 yr, or "million-year," time scales remains an important, open question. We test whether millennial-scale CRN_{DR} erosion rate estimates can be extrapolated to the million-year time scale in the Sierra San Pedro Mártir by comparing predictions for the timing of the onset of normal fault slip based on CRN_{DR} estimates with independent geologic constraints.

2. GEOLOGIC SETTING

2.1 Tectonic Setting

The Sierra San Pedro Mártir is part of the Peninsular Ranges of southern and Baja California (Fig. 2A). It is located in the footwall of an east-dipping, tectonically active normal fault system that forms the western limit of the Gulf of California rift, which is often referred to as the Main Gulf Escarpment (Axen, 1995). The Sierra San Pedro Mártir represents the uplifted rift shoulder and contains the highest topography and relief on the Baja California Peninsula, with local elevations exceeding 3000 m and range relief (summit to base level) ranging from ~500 to 2500 m. The uplifted range front of the Sierra San Pedro Mártir consists of

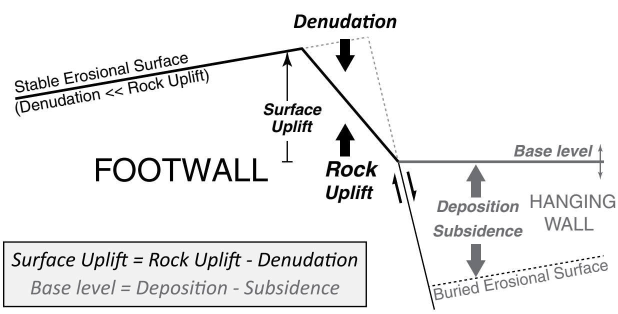

Figure 1. Cartoon illustrating the major vertical fluxes in a simplified cross section of a tilted footwall (4°) offset by a high-angle normal fault (60°) with 2.5× vertical exaggeration. In the footwall, the relief structure of the active escarpment reflects the balance between denudation rates and rock uplift rates relative to base level. If background denudation rates are low with respect to the tectonic forcing, surface uplift of the erosional surface can serve as a structural datum to estimate mean rock uplift rates. Footwall uplift only accounts for a fraction of the total displacement, with the other fraction accommodated by subsidence of the hanging wall (cartoon shows 50-50 balance between uplift and subsidence). Local base level is controlled by the balance between subsidence rates and deposition rates.

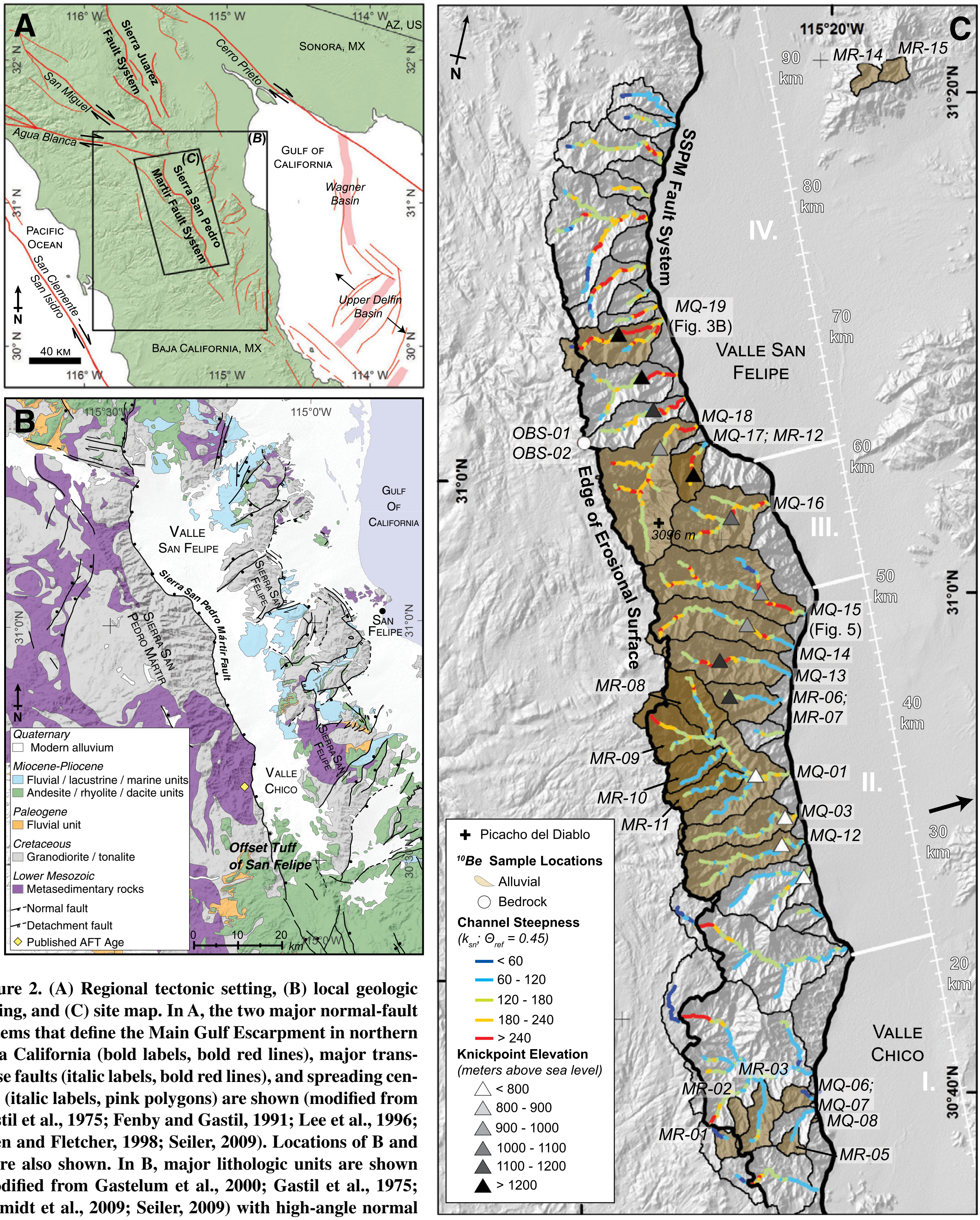

Figure 2. (A) Regional tectonic setting, (B) local geologic setting, and (C) site map. In A, the two major normal-fault systems that define the Main Gulf Escarpment in northern Baja California (bold labels, bold red lines), major transverse faults (italic labels, bold red lines), and spreading centers (italic labels, pink polygons) are shown (modified from Gastil et al., 1975; Fenby and Gastil, 1991; Lee et al., 1996; Axen and Fletcher, 1998; Seiler, 2009). Locations of B and C are also shown. In B, major lithologic units are shown (modified from Gastelum et al., 2000; Gastil et al., 1975; Schmidt et al., 2009; Seiler, 2009) with high-angle normal faults distinguished from rotated detachment faults of the Sierra San Felipe. In C, topographic metrics and sample locations are shown (with descriptions in legend and main text). Samples were collected at the outlets of beige catchments. Other catchments >4 km² used in topographic analysis are outlined in black. The white reference line shows along-strike distances used in Figures 3, 5, and 8 along with labeled fault segments. The black arrow shows external drainage of Valle San Felipe–Valle Chico. MX—Mexico, AZ—Arizona; AFT—apatite fission track; SSPM—Sierra San Pedro Mártir.

Cretaceous granodiorite and tonalite batholith-scale plutons that intrude Paleozoic to Mesozoic metasedimentary and metavolcanic rocks (Fig. 2B; Silver et al., 1969; Gastil et al., 1975; Ortega-Rivera, 2003). In the hanging wall of the Sierra San Pedro Mártir fault, the Valle San Felipe and Valle Chico are synextensional basins that have been infilled with locally derived, late Neogene sediment (Fig. 2B). Further east, the Sierra San Felipe is a series of extended bedrock blocks formerly congruous with the Sierra San Pedro Mártir that have been systematically rotated about horizontal and vertical axes in the hanging wall of the Sierra San Pedro Mártir fault system, suggesting a listric geometry (Stock and Hodges, 1990; Seiler et al., 2010). The Sierra San Pedro Mártir fault system itself is interpreted to be the structurally lowest, breakaway strand of an ESE-directed midcrustal detachment system that has accommodated more than 200 km of tectonic transport since the middle–late Miocene, extending across the Gulf of California from the Sierra San Felipe to Isla Tiburon, near the Sonoran margin (Martín-Barajas et al., 2013). The continuity of this detachment system is broken only in the Delfin basins (Upper and Lower Delfin basins), where ~35 km of new crust have been emplaced since lithospheric rupture at ca. 1–2 Ma (Martín-Barajas et al., 2013). As such, the topographic and structural evolution of the Sierra San Pedro Mártir fault system is integrally tied to the history of rifting in the Gulf Extensional Province as a whole.

2.2 San Pedro Mártir Fault

The NNW-striking Sierra San Pedro Mártir fault system consists of four main arcuate segments that have east-facing concave geometries, and their lateral boundaries are defined by prominent cusps in the mountain front (Fig. 2C). For ease of reference, these segments are numbered consecutively from south to north (I–IV). The entire fault system extends ~100 km along strike, and the length of arcuate segments is 27, 26, 10, and 35 km, respectively, from south to north (Fig. 2C). Segments are subparallel with the overall strike of the range (~325°), with segment III defining a prominent bulge in the Sierra San Pedro Mártir mountain front. Picacho del Diablo (3096 m), the highest peak in Baja California, is located east of the Sierra San Pedro Mártir range crest in the footwall of fault segment III (Fig. 2C). The spatial coincidence of the highest footwall elevation with the shortest fault segment and the absence of abrupt elevation changes at fault segment boundaries imply that the modern footwall topography is not controlled by individual fault segments.

The Sierra San Pedro Mártir fault system is characterized by normal faults that crosscut Quaternary gravels, offset stream channels, have steep scarps up to 25 m high, and are locally associated with well-preserved coseismic landforms such as fissures and free faces, indicating that multiple large earthquakes have occurred along the Sierra San Pedro Mártir fault system during the Holocene (Brown, 1978). Finite slip across the Sierra San Pedro Mártir fault system is best characterized by the offset of a regional, stable erosional surface (Figs. 2C and 3A). The erosional surface is interpreted to be Eocene in age and formed due to the slow beveling of the Cretaceous batholith by river systems sourced from mainland Mexico farther east (Gastil, 1961; Axen et al., 2000). Today, this surface forms a broad, low-relief platform that gently dips (2°–5°) toward the Pacific Ocean and defines the crest of the Main Gulf Escarpment in most places (see Fig. 2C). Elsewhere, small portions of this surface drain to the east across the escarpment itself (e.g., Fig. 3B). Within the Gulf Extensional Province, the same erosional surface is found underlying younger volcanic and sedimentary sequences that cap the tilted fault blocks of the Sierra San Felipe (Seiler et al., 2010). In the Sierra San Pedro Mártir, the erosional surface is not buried, and its eastern edge is clearly defined by a distinct slope break observed in the 30 m digital elevation model. The surface is truncated by rugged topography that reflects the higher denudation rates along the Sierra San Pedro Mártir escarpment (Fig. 2C). We used extracted elevations along this feature as the basis for calculations of

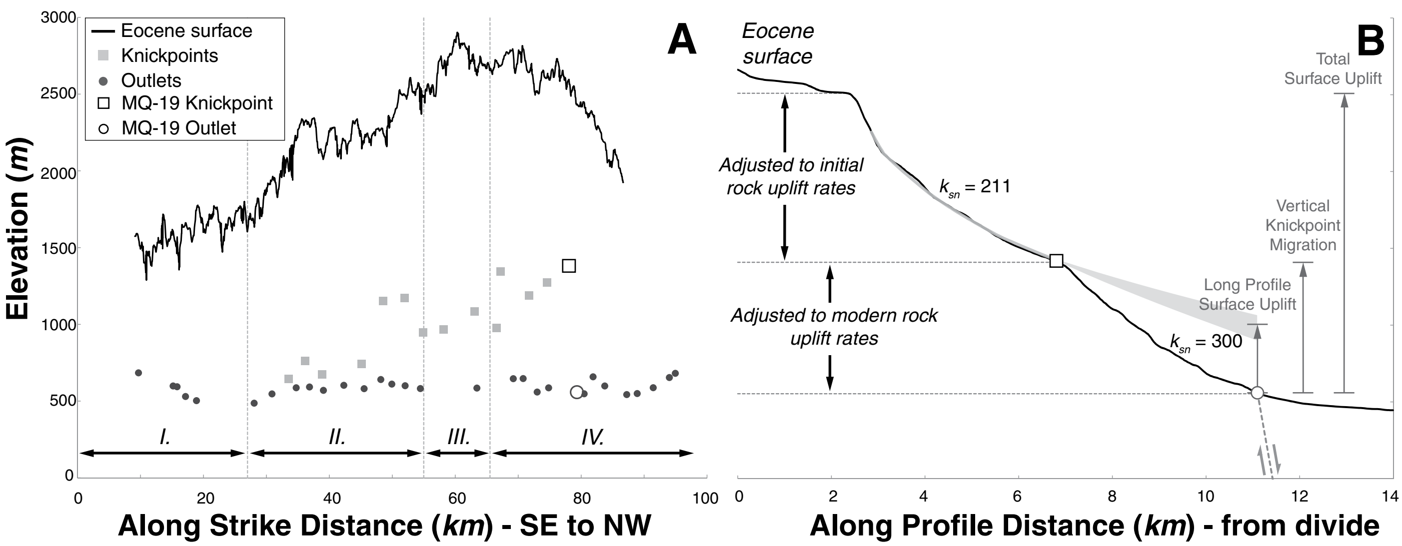

Figure 3. (A) Along-strike elevations of the eastern edge of the Eocene erosional surface, catchment outlets, and prominent slope-break knickpoints, with (B) a corresponding along-profile elevation for the main channel of one catchment. In A, all elevations are projected to the reference line shown in Figure 2C. Fault segments are indicated by dashed vertical lines. In B, the longitudinal profile of MQ-19 illustrates our interpretation of the three erosional domains discussed in the text. Some catchments source small portions of the Eocene erosional surface, but many do not. Many long profiles also have substantial slope-break knickpoints within the escarpment. Downstream of knickpoints, river profiles are graded to higher, modern rock uplift rates, while upstream reaches are interpreted to be graded to slower rock uplift rates associated with early rifting.

accumulated footwall uplift relative to modern base level since the onset of extension (Fig. 1). Footwall uplift only accommodates part of the slip along a normal fault, and the total slip budget requires inclusion of hanging-wall subsidence (Fig. 1). As in other strands of this mid-crustal detachment system (Seiler et al., 2011), maximum subsidence along the Sierra San Pedro Mártir fault system does not coincide with maximum footwall uplift. As such, we made no attempt to reconcile along-strike variations in slip partitioning between the hanging wall and the footwall, and instead we focused exclusively on footwall development relative to the valley floor (Fig. 1). Synthesis of rates and patterns of footwall development with subsidence and sedimentation patterns is an important future research direction.

2.3 Onset of Normal Faulting

The age of initiation along the Sierra San Pedro Mártir fault system is not well constrained. Apatite fission-track ages from the base of the Sierra San Pedro Mártir escarpment are Eocene in age (Gleadow et al., 2003; Schmidt et al., 2009; sample shown in Fig. 2B) and thus predate the ca. 15–9 Ma establishment of plate-boundary shear at this latitude as constrained by global plate reconstructions (Atwater and Stock, 1998). West-tilted middle Miocene volcanic rocks in the hanging wall are unconformably overlain by less-tilted Pliocene conglomerates, suggesting that the onset of extension to the east of the Sierra San Pedro Mártir was post–middle Miocene to pre–early Pliocene (Seiler, 2009). In the southern part of the Sierra San Pedro Mártir fault system, stratigraphic relationships suggest that slip on this part of the fault initiated after eruption of the ca. 12.6 Ma Tuff of San Felipe but before deposition of ca. 6 Ma tuffs (Stock and Hodges, 1989). Near the northern tip of the Sierra San Pedro Mártir fault system, O'Connor and Chase (1989) suggested an age of onset between 2.25 and 5 Ma based on inferred tectonic linkage and consistent slip rates with the Agua Blanca fault. The mechanism of inferred linkage is unclear because the Agua Blanca fault does not reach the Main Gulf Escarpment itself.

3. TECTONIC GEOMORPHOLOGY

3.1 Mean Catchment Hillslope Gradient

Both hillslope and river morphologies encode the tectonics, climate, and lithology of the local setting. However, in high-relief settings, hillslope gradients are limited by rock material strength and are thought to adjust to tectonically driven increases in denudation rates primarily by increasing the frequency of landsliding (Schmidt and Montgomery, 1995; Burbank et al., 1996; Hovius et al., 1998; Montgomery and Brandon, 2002; Larsen and Montgomery, 2012). For 30-m topographic data like that used here (see following), thresholds in catchment-averaged slope for landscapes made up of granitic and metamorphic rocks are between 32° and 37° (e.g., Binnie et al., 2007; Ouimet et al., 2009; DiBiase et al., 2010; Godard et al., 2014; Scherler et al., 2014). To account for this, Roering et al. (1999) proposed a local, nonlinear soil transport model that includes slope thresholds:

$$q_s = \frac{-K_h S}{1-(S/S_c)^2}, \tag{1}$$

where q_s is the sediment flux per unit width (m^2/yr), K_h is a hillslope transport coefficient (m^2/yr) set by the efficiency of soil transport processes, S is local slope, and S_c is a critical slope threshold related to the material strength of the substrate. For uniform denudation rates at topographic equilibrium, mean slope (S_{avg}) can be calculated from this relationship by integrating the local slope values over the mean hillslope length (Roering et al., 2007). Theory-derived predictions of S_{avg} can then be directly compared to observed catchment-averaged values from digital topography.

3.2. Normalized Channel Steepness Index

Several studies have articulated the theory and empirical evidence behind using river longitudinal profiles to infer spatially variable rock uplift rates (for review, see Kirby and Whipple, 2012). As such, we only briefly outline the rationale here. Longitudinal river profiles are commonly well described by Flint's law, relating local slope (S) along a channel profile to its contributing drainage area (A) (Hack, 1957; Flint, 1974):

$$S = k_s A^{-\theta}, \tag{2}$$

where k_s is the channel steepness index, and θ is the concavity index. In this empirical relationship, drainage area above any point along a river is an easily measured proxy for downstream increases in discharge and sediment flux. Concavity indices typically fall within a relatively narrow range of values (~0.4–0.6) for channels that are near topographic equilibrium and are responding to uniform rock uplift rate, uniform rock strength, and spatially uniform runoff (Tucker and Whipple, 2002). Consequently, variations in channel steepness can be directly related to differences in rock uplift rate, rock strength, and/or climate. We adopted the method of Wobus et al. (2006) in choosing a reference concavity (θ_{ref}) to calculate a normalized channel steepness index (k_{sn}). Using normalized channel steepness allows for fair comparison across catchments within a given setting, clear identification of slope-break knickpoints, and direct comparison to analyses done in other geographic settings.

Whether drawing from the stream-power family of fluvial incision models (e.g., Lague et al., 2005) or sediment-flux–dependent ones (e.g., Sklar and Dietrich, 2004), the relationship between k_{sn} and rock uplift rate (U) is well described by a power-law relation at steady state (Gasparini and Brandon, 2011). If θ is invariant with U, as documented in many landscapes (e.g., Kirby and Whipple, 2012), then channel steepness can be directly related to rock uplift rates such that

$$k_{sn} = aU^{\Phi}, \tag{3}$$

where a is a prefactor that includes coefficients of erosional efficiency partially set by climate and lithology, and Φ is a power-law exponent that is affected by the nonlinearity of the incision rule (Whipple and Tucker, 1999) and/or the interaction of erosion thresholds with the discharge variability (DiBiase and Whipple, 2011; Lague et al., 2005).

In such models, transient slope-break knickpoints caused by changes in the rate of rock uplift relative to base level will propagate through the channel network as a kinematic wave (e.g., Rosenbloom and Anderson, 1994; Whipple and Tucker, 1999; Crosby and Whipple, 2006; Berlin and Anderson, 2007; Ellis et al., 2015). Knickpoints will propagate through the river network at a constant vertical velocity that is dependent on the modern rock uplift rate when θ is invariant with U (Niemann et al., 2001). When the incision rule is linear (e.g., Φ = 1), this vertical velocity simplifies to

$$\frac{\Delta z}{\Delta t} = U_{modern}, \tag{4}$$

where Δz is the vertical difference between the knickpoint elevation and base level, Δt is the time since the rock uplift rate has changed, and U_{modern} is the modern rock uplift rate. Equation 4 can be rearranged to solve for Δt and used to determine the age of the change in rock uplift rate. Possible causes for a change in rock uplift rates include the initiation of normal faulting (i.e., where Δz is the difference between a knickpoint defining the edge of the Eocene erosional surface and base level) and the age of an

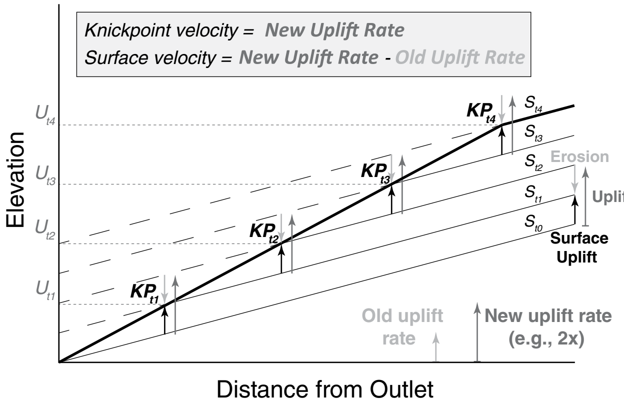

Figure 4. Schematic plot of channel long profile evolution responding to a change in rock uplift rates. U marks rock uplift, S marks surface elevation, and KP marks knickpoint elevations for constant time-step intervals (subscripts; t1–t4 where t0 is the initial condition). At t0, the constant gradient profile is adjusted to old rock uplift rates and thus erosion rates equal old rock uplift rates (light gray arrows). For a doubling of rock uplift rates (medium gray arrows), the steady state profile is also doubled in this simplified geometry (bold, solid line at S_{t4}). At each time step in between, surface uplift (black arrows) of the channel profile above the knickpoint is the rock uplift minus erosion. Downstream of the knickpoint, surface uplift is equal to zero (projections of the paleo-channel profile are shown as long, dashed lines). This figure geometrically illustrates how knickpoint velocity is only a function of the new rock uplift rate (short, dashed lines added for clarity to show that U and KP elevations are the same for a given time step) while surface uplift velocity of the initial channel profile is the difference between new rock uplift rates and old ones.

increase in rock uplift rates (or base-level drop) that generated slope-break knickpoints (i.e., where Δz is the difference between the modern knickpoint elevation and base level). Under this view, channel reaches upstream of knickpoints are equilibrated to old uplift rates, while reaches downstream are equilibrated to modern ones (see Fig. 3B for an example).

Equation 4 states that the vertical knickpoint velocity depends only on new (modern) rock uplift rates. In contrast, surface uplift of the long profile above the knickpoint is set by the difference between new and old rock uplift rates. Figure 4 graphically illustrates this phenomenon using (simplified) constant-gradient long channel profiles. The arrows in Figure 4 are scaled to an old (initial) rock uplift rate and a new (modern) rock uplift rate. The solid line labeled S_{t0} (i.e., channel surface at time, t0) represents a lower steady-state channel gradient for the old rock uplift rate (1×), and the bold, solid line labeled S_{t4} (i.e., channel profile after four time steps) represents a higher steady-state channel gradient for the new rock uplift rate (2×). At each time step in Figure 4, the old channel profile is uplifted and eroded according to the new and old uplift rates, respectively. This occurs until passage of the knickpoint, below which the channel has adjusted to the higher steady-state gradient for the new rock uplift rate (Fig. 4). Vertical knickpoint velocity equals the new rock uplift rate, and knickpoint elevation records the accumulated uplift that has occurred at this new rate. This result holds for any combination of old uplift rate, new uplift rate, and initial steady-state channel gradient. The knickpoint elevation increases faster than surface uplift of the old channel profile because the surface is uplifting at the same time that knickpoint position is laterally migrating upstream. The analysis of Niemann et al. (2001) demonstrated that the same results hold for concave river profiles where steady-state channel geometries are described by channel steepness instead of a constant channel gradient.

4. METHODS

4.1 Topographic Analysis

For each catchment along the Sierra San Pedro Mártir fault system, we calculated a number of morphometric parameters in ArcGIS™ using a digital elevation model (DEM) acquired through the Shuttle Radar Topography Mission (SRTM; Farr et al., 2007). Calculated parameters include drainage area, elevations at the edge of the Eocene erosional surface that define the top of the Sierra San Pedro Mártir escarpment, outlet elevation, slope-break knickpoint elevations (if present), total catchment relief, catchment-averaged hillslope gradient (S_{avg}), catchment-averaged local relief measured over a 2.5-km-radius window, catchment-averaged normalized channel steepness index (k_{sn}), and a best-fit overall channel concavity (θ). All calculations except 2.5 km local relief were determined from the raw 1 arcsecond (~30 m) SRTM data set hosted at the Jet Propulsion Laboratory. Holes in the raw data were filled using nearest neighbor interpolation in order to generate flow accumulation grids, but they are not included in the catchment-averaged statistics reported in Table 1 and supplementary tables found in the Data Repository.[1] Local relief measured over a 2.5 km radius was calculated from the globally available, 3 arcsecond (~90 m) finished DEM derived from the SRTM data (v4), processed and hosted at Consultative Group on International Agricultural Research (CGIAR; http://www.cgiar-csi.org/). For catchment-averaged metrics, any portions of catchments that were located on the Eocene erosional surface (i.e., above the knickpoint at the top of the escarpment; e.g., Fig. 3B) were excluded from catchment-averaged statistics because they have not yet responded to changes in base level caused by Sierra San Pedro Mártir normal faulting.

For each 30 m pixel in the DEM, hillslope gradients represent the maximum descent to any of the neighboring eight pixels (i.e., D8 slope). Catchment relief is the difference between the highest and lowest elevations in each watershed and provides an estimate of accumulated surface uplift for catchments draining the Eocene erosional surface. However, catchment relief is strongly dependent on drainage area and the presence of prominent peaks. To avoid this drainage area dependence and include more catchments in the topographic analysis, we calculated local relief over a 2.5 km radius following the lead of prior studies (e.g., Ahnert, 1970; Montgomery and Brandon, 2002), and we report catchment-averaged values of local relief for each catchment. Catchment-averaged local relief calculated over a uniform radius can be marginally biased by including elevations outside of watershed boundaries, but it has proven to be an effective measure of local relief that is sensitive to increases in denudation rates beyond

[1]GSA Data Repository item 2016296, provides tables summarizing the topographic analyses used to construct Figure 8 (DR1) and to determine the difference between predictions using one-stage versus two-stage models of fault initiation (DR2), is available at http://www.geosociety.org/pubs/ft2016.htm or by request to editing@geosociety.org.

TABLE 1. COSMOGENIC RADIONUCLIDE (CRN) SAMPLE LOCATIONS, MORPHOMETRICS, AND DENUDATION RATES

Sample	Longitude (°W)	Latitude (°N)	Mean elevation (m)	Drainage area (km^2)	Effective elevation (m)	Knickpoint elevation (m)	Catchment relief (m)	2.5 km relief (m)	Mean slope	Channel steepness (m$^{0.9}$)	1σ* (m$^{0.9}$)	^{10}Be/SiO$_2$ (at/g)	1σ (at/g)	CRN$_{DR}$ (m/m.y.)	1σ (m/m.y.)	t_{avg}† (k.y.)
Alluvial samples—Sierra San Pedro Mártir footwall																
MQ-01§	115.3108	30.8557	1520	80.50	1575	743	2011	1124	28.7	136	3	80278	26790	122	47	4.9
MQ-03	115.2686	30.8103	1346	21.81	1397	675	1763	1035	26.9	134	4	66775	13513	133	30	4.5
MQ-06#	115.1740	30.6381	827	3.85	833	N/A	1387	784	23.8	52	5	88872	14323	72	13	8.4
MQ-07#	115.1731	30.6383	813	4.06	820	N/A	641	780	23.4	56	4	31742	17664	206	67	2.9
MQ-08	115.1541	30.6258	740	0.16	740	N/A	231	852	21.4	N/A	N/A	84958	19657	71	18	8.4
MQ-12	115.2659	30.7866	1416	24.83	1472	763	1759	1051	28.8	134	3	69849	18272	133	39	4.5
MQ-13	115.3093	30.9202	1485	27.80	1570	1173	1996	1290	28.6	169	14	82942	18314	118	29	5.1
MQ-14	115.3237	30.9428	1603	31.44	1685	946	2108	1295	31.2	162	7	75329	16109	139	33	4.3
MQ-15	115.3254	30.9728	1638	45.48	1713	968	2439	1325	28.9	165	8	86237	18820	123	30	4.9
MQ-16	115.3409	31.0135	1638	30.16	1707	1085	2437	1557	33.6	188	8	57918	8218	184	30	3.3
MQ-17	115.3725	31.0418	1521	9.23	1575	1345	1769	1616	32.6	197	23	74468	18249	132	36	4.5
MQ-18	115.4074	31.0242	1899	51.91	1971	978	2374	1522	34.9	200	4	59163	19032	209	77	2.9
MQ-19	115.4604	31.1146	1789	21.47	1879	1381	2222	1453	30.6	234	13	33579	10068	353	119	1.7
MR-01	115.2246	30.5973	1579	3.42	1582	N/A	374	862	14.8	48	5	106901	5345	85	7	7.1
MR-02	115.2184	30.6179	1147	3.49	1159	N/A	801	979	25.7	80	13	103585	7251	69	7	8.8
MR-03	115.2001	30.6177	1124	11.13	1144	N/A	1074	881	25.8	107	5	93005	5580	76	7	7.9
MR-05	115.1696	30.6073	1045	3.04	1039	N/A	651	879	26.2	78	5	64891	4542	104	10	5.8
MR-06**	115.1696	30.6073	1207	13.39	1234	N/A	1387	1127	28.5	123	6	96511	8686	77	9	7.8
MR-07**	115.2858	30.8959	1207	13.39	1234	1151	1387	1127	28.5	123	6	53033	6364	143	20	4.2
MR-08§	115.3286	30.8890	1720	15.39	1757	N/A	1559	1214	27.7	134	6	89972	5398	112	11	5.3
MR-09§	115.3434	30.8662	1817	18.47	1852	N/A	1371	1188	32.0	160	4	105540	8443	101	11	5.9
MR-10§	115.3181	30.8439	1564	9.58	1596	N/A	1404	1203	30.0	107	3	77556	61269	119	34	5.0
MR-11§	115.3036	30.8327	1428	10.45	1467	N/A	1477	1110	27.4	115	4	94079	70559	91	27	6.6
MR-12	115.3728	31.0411	1536	8.97	1584	N/A	1728	1625	32.9	210	24	60713	4250	152	15	3.9
Alluvial samples—Sierra San Pedro Mártir hanging wall																
MR-14	115.2925	31.3285	1005	3.47	1008	N/A	440	624	24.1	47	2	216069	8643	29	2	20.5
MR-15	115.2692	31.3370	891	3.66	896	N/A	530	648	23.6	64	10	155758	9345	39	4	15.5
Bedrock samples																
OBS-01	115.4660	31.0462	2784	N/A	N/A	N/A	N/A	N/A	N/A	N/A	N/A	3673883	134576	4.73	0.45	126.8
OBS-02	115.4655	31.0459	2792	N/A	N/A	N/A	N/A	N/A	N/A	N/A	N/A	2370973	170839	7.63	0.87	78.6

*1 standard error about the mean.

†t_{avg} is the time required to erode ~0.6 m of bedrock (i.e., the characteristic depth of cosmogenic production of ^{10}Be).

§MR-08, MR-09, MR-10, and MR-11 are nested samples within MQ-01.

#MQ-06 is a nested sample within MQ-07 that was collected upstream of a series of small bedrock steps in the active channel.

**MR-06 and MR-07 are replicate samples taken from different deposits in the active channel.

slope thresholds (e.g., DiBiase et al., 2010). The appropriate length scale for calculating local relief varies from landscape to landscape, but we find that a 2.5 km radius is adequately large to capture ridge-valley spacing and small enough to minimize undue influence from neighboring watersheds in the calculation of catchment-averaged values.

To identify slope-break knickpoints and calculate channel steepness, we used automated, freely available scripts for Matlab and ArcGIS™ (http://www.geomorphtools.org). We identified knickpoints manually using prominent slope breaks in slope-area plots. Normalized channel steepness values used a $\theta_{ref} = 0.45$ (e.g., Wobus et al., 2006) to determine a reach-averaged k_{sn} for all 500 m reaches draining an area of >1.5 km^2 downstream of the edge of the Eocene erosional surface. We found that maintaining this critical area guaranteed that we were within the graded portion of the channel network and beyond local oversteepening of channel profiles immediately downstream of slope-break knickpoints marking the edge of the Eocene erosional surface (for comments on this common phenomenon, see Berlin and Anderson, 2007; Kirby and Whipple, 2012). We determined k_{sn} by averaging all reaches within the catchment, and we report one standard error about the mean in Table 1. Mean overall channel concavities were estimated by fitting the main-stem channel from below the Eocene surface to the range-front outlet. In catchments with slope-break knickpoints and where downstream reaches below knickpoints were well graded (i.e., reaches were long enough to characterize a clear slope-area scaling relationship), we also used the functional relationship between k_{sn} and CRN_{DR} (see following) to infer downstream denudation rates. As in the determination of catchment-averaged k_{sn}, we used 500 m reach averages to calculate mean k_{sn} above and below knickpoints. For downstream sections, we excluded segments immediately adjacent to the knickpoint, which are often influenced by abrupt steps and waterfalls (Berlin and Anderson, 2007; Kirby and Whipple, 2012) and can artificially inflate values of mean $k_{sn.}$

4.2 Cosmogenic ^{10}Be Denudation Rates

In this study, cosmogenic radionuclide–derived denudation rates (CRN_{DR}) were based on in situ cosmogenically produced ^{10}Be in quartz. Production of ^{10}Be varies as a function of latitude, elevation, and time. For a given production rate, concentrations of ^{10}Be can be inverted to determine average surface denudation rates over 10^2–10^5 yr time scales (Lal, 1991). Catchment-averaged denudation rates were measured by amalgamating alluvial quartz sands collected at the drainage outlet (Bierman and Steig, 1996; Granger et al., 1996). The catchment-averaged approach assumes that river transport naturally samples quartz from the entire watershed and that alluvial sands are well mixed and not systematically biased toward a single source area. We followed best practices in sampling based on prior studies that also measured gradients in denudation rates in steep, tectonically active landscapes (Cyr et al., 2010; DiBiase et al., 2010; Godard et al., 2014; Harkins et al., 2007; Ouimet et al., 2009; Scherler et al., 2014). For example, geologic and analytic uncertainties associated with the CRN_{DR} method are minimized by measuring large numbers of alluvial samples from well-graded fluvial catchments of modest size (~5–500 km^2). In this work, we collected alluvial samples from 26 catchments (Fig. 2C) over two separate field campaigns (distinguished by MQ and MR sample identifiers). The MR sampling strategy was designed after the collection of MQ samples to include a suite of nested and replicate samples to help us evaluate the extent to which alluvial sediments are well mixed in the Sierra San Pedro Mártir. Twenty-four alluvial samples were from the eastern escarpment of the Sierra San Pedro Mártir fault system itself. Two additional alluvial samples (MR-14, MR-15) were from a low-relief, uplifted block in the hanging wall in the northern Sierra San Felipe and were collected to supplement observations in the Sierra San Pedro Mártir with areas of low topographic relief and low channel steepness, but with similar climate and lithology. None of the catchments showed any evidence of Quaternary glaciation. Samples were collected from small fluvial bars or filled pools deposited in the active channels of major ephemeral streams that drain into the Valle de San Felipe–Valle Chico basin. Field estimates of active channel widths ranged from ~2 to 20 m. We avoided portions of the channels adjacent to alluvial terraces or nearby slope failures to minimize potential biasing of CRN concentrations due to local sediment input and reworking. All samples came from channels dominated by granitoid alluvium ranging in size from fine-grained sand to subrounded boulders >1 m in diameter.

We collected replicate (repeat measurements at the same location) and nested (subcatchments within a larger catchment) samples to address potential complications associated with stochastic landslide inputs (Niemi et al., 2005; Yanites et al., 2009) in a seismically active zone (Quigley et al., 2007) and heterogeneous lithology in the central portion of the range (Fig. 2B). This included four nested samples across a lithologic contact, one nested sample above and below a minor knickzone, and two replicate samples (see Fig. 2C). The four nested catchments (MR-08, MR-09, MR-10, and MR-11, all within MQ-01) were sampled across a transition from granitoid to metasedimentary lithologies, but all contained a large amount of alluvial quartz sand. One nested sample was also collected above and below a minor knick zone with ~12 bedrock steps, ~2–5 m height each, spaced ~20–30 m apart (MQ-06, MQ-07), in a steeply incised bedrock gorge near the Sierra San Pedro Mártir range front. The two sets of replicate samples were collected from different bars of sediment within the active channel (MR-06, MR-07) and across field campaigns (MQ-17, MR-12). One alluvial sediment sample was from a catchment too small to allow accurate determination of topographic metrics (MQ-08), and it was consequently excluded from analyses relating morphometrics with CRN_{DR}. We used the nested and replicate samples to better constrain geologic uncertainty in interpreting millennial-scale denudation rates in the Sierra San Pedro Mártir.

We collected two bedrock samples from the Sierra San Pedro Mártir range crest (Fig. 2C) for CRN_{DR} to complement alluvial samples and constrain "background" denudation rates of the Eocene erosional surface. The low relief of the Eocene erosional surface suggests that it is not yet responding to the base level of the tectonically active escarpment forming the eastern margin of the Sierra San Pedro Mártir. As such, denudation rates from the range crest should provide an estimate of erosional lowering of the Eocene erosional surface that spans beyond the averaging time scales of denudation rates along the active Sierra San Pedro Mártir range front. Bedrock samples were chiseled from the uppermost 1 cm of intact, porphyritic granite bedrock on horizontal surfaces exposed along the peak of the escarpment (Fig. 2C). Each sample was amalgamated from individual rock chips that were collected over an ~3 m^2 surface. Surfaces showed evidence for lichen growth, centimeter-scale exfoliation, pitting, and dissolution weathering, implying slow, in situ weathering over many thousands of years. At both sampling sites, there was no evidence for removal of large blocks due to, for instance, frost heave, coseismic mass wasting, or human activity.

Samples from the different field campaigns were processed (i.e., quartz separation and purification; Be extraction) in different laboratories—MQ samples at the University of Melbourne Cosmogenic Radionuclide Laboratory and MR samples at the WOMBAT Laboratory at Arizona State University. Bedrock samples were first crushed and milled. Alluvial samples for MQ and MR were sieved to isolate the 0.25–0.50 mm and 0.25–1.0 mm size fraction, respectively, in order to minimize effects of varying grain size on calculated denudation rates. Quartz separation and ^{10}Be isolation were done using standard techniques (Kohl and Nishiizumi, 1992). We processed laboratory blanks in tandem with samples in both laboratories, and concentrations reported in Table 1 have been blank corrected. The ^{10}Be measurement for MQ and MR samples were also done on different accelerator mass spectrometers—MQ samples at the 14UD accelerator at Australian National University and MR samples at PrimeLab at Purdue University.

For bedrock samples, shielding related to topography and sample geometry was computed using the CRONUS geometric shielding calculator (http://hess.ess.washington.edu/math/general/skyline_input.php). Scaling factors along with other site characteristics (Table 1) were entered into version 2.2 of the CRONUS cosmogenic calculator (http://hess.ess.washington.edu/) to determine in situ bedrock erosion rates (Balco et al., 2008). For catchment-averaged samples, we followed the approach taken by Portenga and Bierman (2011) such that denudation rates are directly comparable to their global compilation of CRN_{DR}. Using 90 m DEMs, we calculated spallation production rate scaling factors as a function of latitude, longitude, and elevation for each pixel within a catchment. The average production rate from this analysis was used to find the equivalent latitude-longitude-elevation triad to enter into the CRONUS calculator. To maintain consistency with the Portenga and Bierman (2011) data set, we used a standard topographic shielding factor of 1. CRN_{DR} values were only reduced by 2%–3% if catchment-averaged hillslope was used to calculate a topographic shielding factor, instead of using the default shielding factor of 1. This is insignificant compared to the propagated error in CRN_{DR} resulting from analytic uncertainties in ^{10}Be concentrations and uncertainties in ^{10}Be spallation and muogenic production rates (Balco et al., 2008).

5. RESULTS

5.1 Catchment Morphometry along the Sierra San Pedro Mártir

Figure 3A shows the range-front outlet elevations that define modern base level together with the elevations of the top of the escarpment as defined by the eastern margin of the Eocene erosional surface. Using escarpment relief as a proxy for accumulated footwall uplift relative to base level, the Sierra San Pedro Mártir broadly conforms to theoretical expectations of along-strike gradients in total displacement for normal-fault blocks (Cowie and Scholz, 1992; Dawers et al., 1993), albeit with a more asymmetric character than the simplified conceptual model. Slope-break knickpoints are observed in many drainages throughout the central portion of the Sierra San Pedro Mártir escarpment, and their elevations increase systematically toward the north, mimicking the increase in escarpment relief (Fig. 3A). Because knickpoint elevations are a proxy for accumulated uplift due to modern, accelerated rock uplift rates relative to base level (Fig. 4; Niemann et al., 2001), Figure 3A demonstrates that a significant proportion of the total relief was generated during the later phase of faster uplift. Figure 3B provides an illustrative example (MQ-19) of how catchments in the Sierra San Pedro Mártir display distinct topographic expressions of these three erosional regimes: (1) a prerifting, relict Eocene erosional surface; (2) post-Eocene response to Sierra San Pedro Mártir normal faulting; and (3) recent transient response to increases in rock uplift rates relative to base level. Catchment-averaged statistics reported in Figure 5 include both regimes 2 and 3 where observed and should be interpreted accordingly.

Figure 5 summarizes how other measures of topography in the Sierra San Pedro Mártir vary along strike (also in Table DR1 [see footnote 1]). The size of points is scaled to drainage area to visually assess whether variations in other morphometrics are dependent on drainage area. Drainage area is highly variable along strike, with the largest watersheds found in the southern portion of the range (Fig. 5A). Outlet elevations decrease from >650 m in the southern (10–20 km) and northern tips (90–100 km) of the Sierra San Pedro Mártir fault system to a mean elevation of ~580 m between 20 and 90 km (Fig. 5B). Heterogeneous subsidence patterns and drainage systems within the hanging-wall basin influence local outlet elevations, but this variation constitutes a negligible contribution to catchment relief and accumulated surface uplift relative to base level.

Four of the metrics shown in Figure 5 measure relief and topographic "ruggedness" of catchments of the Sierra San Pedro Mártir escarpment: catchment relief (Fig. 5E), mean catchment hillslope angle (Fig. 5F), normalized channel steepness (Fig. 5G), and mean 2.5-km radius local relief (Fig. 5H). Catchment relief (Fig. 5E) largely mirrors the along-strike asymmetry in surface uplift of the Eocene erosional surface (Fig. 3A) when small catchments that do not drain the divide are excluded. A notable exception is one catchment in segment III that drains Picacho del Diablo, which is the highest peak in the Sierra San Pedro Mártir and is located east of the Sierra San Pedro Mártir range crest. Catchment-averaged local relief measured over a 2.5 km radius removes the scale dependency of watersheds with different drainage areas. Accordingly, all catchments, including those not draining the divide, follow the same asymmetrical trend along strike (Fig. 5H). Both catchment and local relief attain maximum values near the boundary between Sierra San Pedro Mártir fault segments III and IV (km 63–67; see Fig. 2C), north of the geometric center of the fault system (km 50; see Fig. 2C). A similar along-strike asymmetry is observed in catchment-averaged hillslope gradient, S_{avg} (Fig. 5F) and catchment-averaged normalized channel steepness, k_{sn} (Fig. 5G). Peak k_{sn} values occur farther north (km 78; see Fig. 2C) than the maxima of other parameters and correlate more closely with the northward increases in knickpoint elevations shown in Figure 3A.

Mean channel concavity (θ) spans a relatively narrow range of values (mean θ = 0.43) in segments I and II (Fig. 5C), consistent with the expected range of 0.4–0.6 for well-equilibrated channels subjected to uniform rock uplift (Tucker and Whipple, 2002) and empirically observed in other actively denuding settings (Duvall et al., 2004; Kirby and Whipple, 2001; Snyder et al., 2000; Wobus et al., 2006; Adams et al., 2016). However, in segment III and the southern section of segment IV, concavities are systematically reduced to near zero (Fig. 5C). These low-concavity indices reflect the presence of slope-break knickpoints, where channels steepen downstream and descend rapidly to the range front (Figs. 3B and 6B). In fact, when channel concavities are measured only upstream of prominent knickpoints, they exhibit a more typical range of concavities from ~0.4 to 0.6. Importantly, slope-break knickpoints do not coincide with geologic contacts, giving us confidence in the interpretation of knickpoints as a transient response to increased rock uplift rates relative to base level.

We also identified a topographic bench at the boundary between segments II and III, which we interpret as an uplifted bedrock or alluvial surface that likely formed at base level. Figure 6 shows the morphology of the catchment (MQ-15) associated with this uplifted bench (Fig. 6C). Hillslope gradients are steeper below the prominent knickpoint at ~400 m above base level (white star; Fig. 6A), and the main-stem channel is well graded upstream of this knickpoint (Fig. 6B). The lowermost tributary of MQ-15 is not well graded to the main stem (Fig. 6B) and may be an example of how large landslides or drainage capture events influence longitudinal profiles in this setting, especially for smaller drainage areas. Importantly, the elevation of the bench is substantially lower than

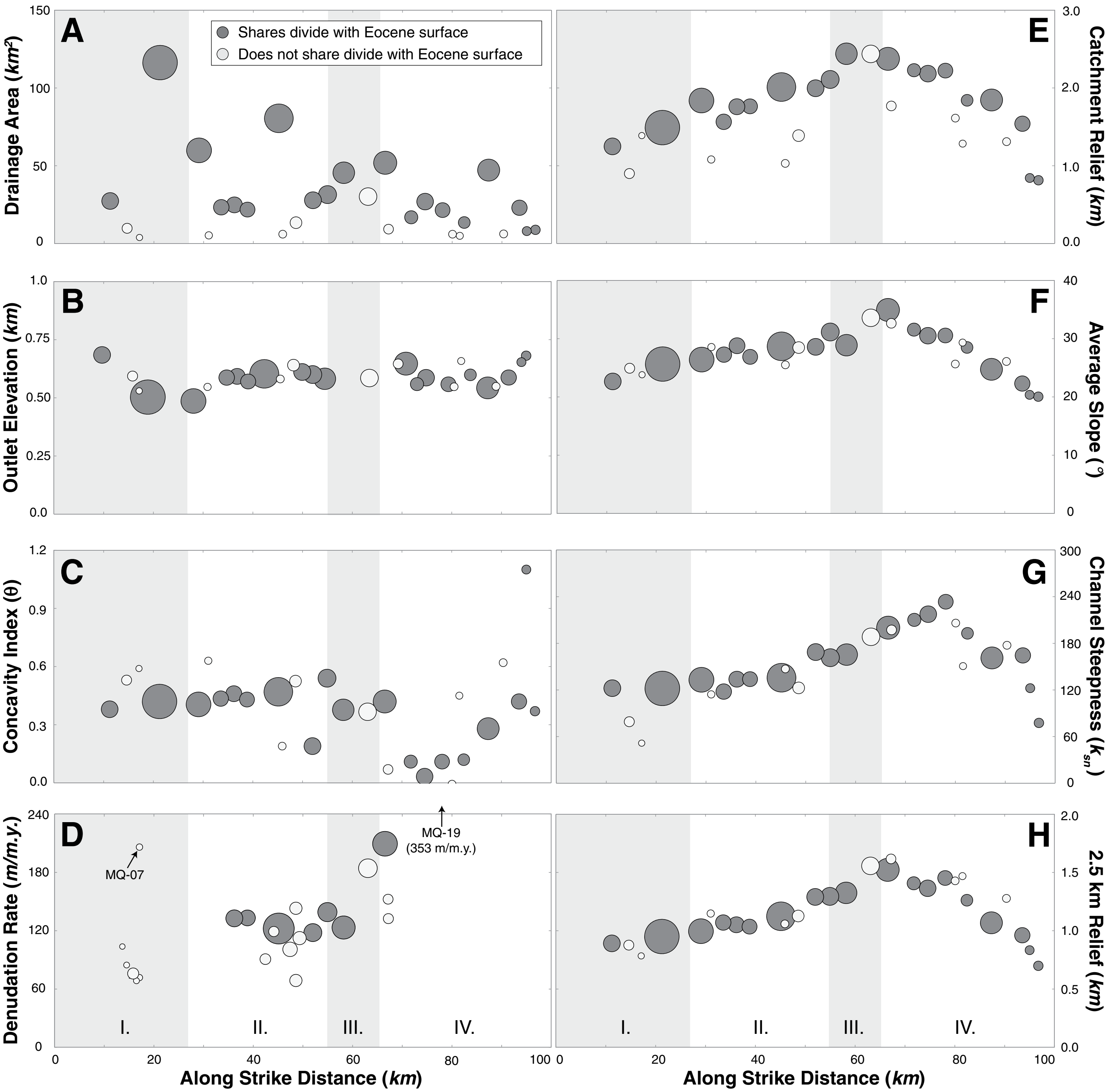

Figure 5. Schematic plot of channel long profile evolution responding to a change in rock uplift Figure 5. Along-strike variations in morphology for all catchments >4 km² that drain across the Sierra San Pedro Mártir fault system: (A) drainage area, (B) outlet elevation, (C) mean channel concavity, (E) total catchment relief, (F) catchment-averaged slope, (G) catchment-averaged normalized channel steepness, and (H) catchment-averaged 2.5-km-radius local relief. (D) Cosmogenic ^{10}Be denudation rates are also shown for alluvial samples collected within the Sierra San Pedro Mártir, though not all samples were collected at the range front (see Fig. 2C). Two potential outliers (MQ-07, MQ-19) are also labeled for reference (see Fig. 7). Catchments that share a divide with the Eocene erosional surface are distinguished from those that do not. Marker size is scaled by drainage area (scaling shown in A), and fault segments are indicated by alternating white and gray shading. For all but B, the centroid of the catchment has been projected to the reference line shown in Figure 2C because they represent mean catchment properties. For B, the actual outlet position has been projected to the reference line.

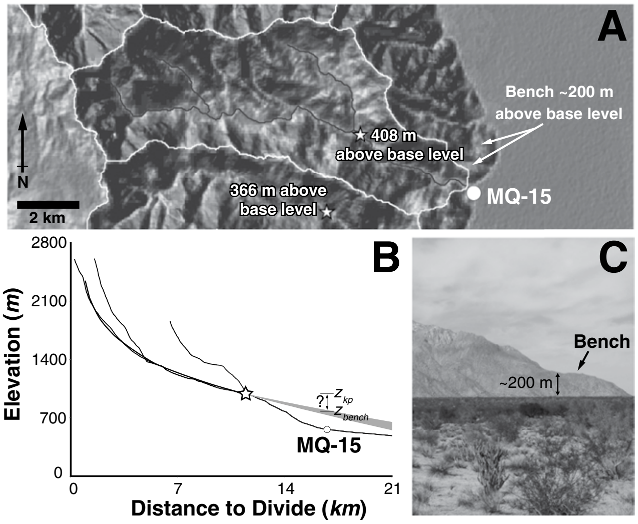

Figure 6. (A) Slope draped over a shaded relief map, (B) channel long profiles for MQ-15, and (C) a photo of an uplifted bench at the range front. In A, high slopes are dark and low slopes are light. The extent of the uplifted fan/bedrock surface can be seen in map view (~200 m above local basin fill) and is preserved where segments II and III linked. In B, the projection of the channel profile upstream of a knickpoint (solid gray line) is extrapolated downstream (where gray shading shows range of concavity from 0.45 to 0.6). Plausible explanations for the mismatch between knickpoint elevation (z_{kp}) and the uplifted bench (z_{bench}) are discussed in the main text.

the slope-break knickpoint elevation (Fig. 6B), suggesting either that there is nonuniform uplift near the range front, uplift there is partitioned among multiple fault strands, the bench formed after the recent increase in rock uplift rates, and/or the bench eroded substantially since formation.

5.2 In Situ Bedrock Denudation Rates

All parameters used to calculate in situ and alluvial CRN_{DR} are reported in Table 1. We also report "averaging time scales" for samples (t_{avg}). These refer to the time required to erode ~0.6 m of bedrock (i.e., the characteristic depth of cosmogenic ray penetration relevant to CRN production) and were calculated using the CRN_{DR}. Assuming steady-state denudation, these ages represent a minimum integration time over which the calculated rates are representative. CRN_{DR} of bedrock surfaces at the Sierra San Pedro Mártir summit are 4.7 ± 0.5 and 7.6 ± 0.9 m/m.y. (Table 1). Given the weathering characteristics of the summit surfaces and lack of any evidence for spallation of blocks of >1–2 cm thickness, we interpret these findings to reflect steady-state bedrock denudation rates associated with lowering of the Eocene erosional surface. Averaging time scales of summit samples are ~127 and 79 k.y. (Table 1). As such, they provide an integrated record of bedrock erosion that spans the Last Glacial Maximum and, in the former case, the Last Interglacial Period. Given that glacial-interglacial cycles have operated in a similar fashion throughout the Quaternary, we suspect that the bedrock erosion rates we calculated may be reasonable estimates of background lowering rates of the Eocene erosional surface over at least the last 3–2 m.y.

5.3 Catchment-Averaged Denudation Rates

We report 26 new catchment-averaged denudation rates (CRN_{DR}) in Table 1 with rates that range from 69 ± 7 m/m.y. to 353 ± 119 m/m.y., with a mean value of 130 ± 30 m/m.y. Associated averaging time scales range 1.7 ≤ t_{avg} ≤ 8.8 k.y. and thus represent denudation rates spanning the Holocene. Two other samples were collected away from the escarpment in the hanging wall of the Sierra San Pedro Mártir fault system in a low-relief, uplifted granitic block of the northern Sierra San Felipe. These samples have a mean CRN_{DR} of 34 ± 3 m/m.y. (t_{avg} ~17.6 k.y.) and are useful to better constrain the k_{sn}-CRN_{DR} relationship developed below (see section 6.1). CRN_{DR} sample density is higher in the central and southern portions of the Sierra San Pedro Mártir, where catchments are largely composed of granitoid lithologies, though including variable proportions of metasedimentary rock (Fig. 2B). In general, CRN_{DR} values are systematically higher in the central portions of the range (Fig. 5D), consistent with concomitant increases in catchment relief.

Four samples (MR-08, MR-09, MR-10, MR-11) nested within MQ-01 allow us to check the assumption that sand grains are well mixed and representative of the entire catchment. They also provide a test for whether there is an obvious lithologic bias between metamorphic and granitic catchments in the Sierra San Pedro Mártir that could affect the relationship between morphometrics and denudation rates. Quantification of the relative source areas of different lithologies is approximate and estimated from the geologic map shown in Figure 2B, which was compiled using published geologic maps (Gastelum et al., 2000; Gastil et al., 1975; Schmidt et al., 2009; Seiler, 2009). Despite lithological variation, the average CRN_{DR} values of these four nested catchments differ from the values of the entire catchment (MQ-01) by <15% (Table 1) and are within analytical uncertainties. Two subcatchments (MR-08, MR-09) have slightly steeper channel profiles (mean k_{sn} ~145 compared to ~110) and are more uniformly granitic (>90% compared to ~50% granitic) but show similar mean hillslopes (S_{avg} ~30° compared to 29°) to the other two subcatchments (MR-10, MR-11). Mean CRN_{DR} values for both of these lithologically defined subsets are ~105 m/m.y. There is an ~25% difference in mean channel steepness and ~5% difference in mean hillslope gradients among these two subsets. As such, we conclude that lithological differences produce a <25% effect in equilibrium channel steepness (k_{sn}) and a <5% effect in catchment-averaged slopes (S_{avg}). Although this complication may contribute to the sharp increase in k_{sn} values seen at kilometer 45 (Fig. 5G), it does not explain the overall asymmetry observed (i.e., that peak channel steepness is skewed toward the north). Furthermore, given that mean 1σ analytical uncertainties on CRN_{DR} in the Sierra San Pedro Mártir are ~20%, we find that geologic sources of uncertainty due to uniform mixing assumptions and heterogeneous lithology are of similar magnitude to analytical uncertainties.

To reliably use CRN_{DR} data to test functional relationships between morphology and long-term denudation rates, large numbers of samples are required to overcome both the geological and analytical sources of uncertainty inherent to the approach. The hazard of over-interpreting individual CRN_{DR} rates is emphasized by one set of replicate samples and one set of nested samples collected in this study. In the first case, replicate samples were taken from fluvial deposits in the active channel at slightly different levels (MR-06 = 77 ± 9 m/m.y. and MR-07 = 143 ± 20 m/m.y.) and show that sand delivered to the channel during different flow events can lead to an almost 2× difference in inferred denudation rates, well outside analytical uncertainties. There are no grounds to ignore either observation, so both are included in subsequent analyses. In the second case, a set of nested samples collected immediately above (MQ-06) and below (MQ-07) a series of small bedrock steps in the active channel shows a dramatic reduction in ^{10}Be concentrations in stream sediments that correspond to an apparent downstream increase in CRN_{DR} from 72 ± 13 to 207 ± 67 m/m.y. MQ-07 was collected ~20 m downstream of this minor knick zone, near exposed abundant, small rockfall deposits, which likely contributed material with low ^{10}Be concentration that gave rise to this anomalously high denudation rate. It is worth noting that other samples in this study were collected away from local cut banks and rockfall zones and either above or substantially downstream of major knickpoints. CRN_{DR} values show no clear bias due to oversteepened reaches in these watersheds. This is likely due to the fact that they were collected far enough downstream to allow adequate mixing. Nevertheless, the highest denudation rate (353 ± 119 m/m.y.) did come from a catchment with a prominent knickpoint (MQ-19; Fig. 3B), where the active stream channel of MQ-19 consists of an abundance of large (>10-m-diameter) angular to subrounded boulders, and where catchment S_{avg} and k_{sn} are the highest in this study, thereby making it susceptible to the stochastic delivery of deep-seated landslides (Niemi et al., 2005). As such, evaluating whether or not this rate is representative of the long-term (>10^4–10^6 yr) catchment denudation rates is difficult based on available data.

6. ANALYSIS AND DISCUSSION

While observed denudation rates from the Sierra San Pedro Mártir summit surfaces are low, they are consistent with global averages of in situ denudation rates of igneous bedrock lithologies (8.7 ± 1.0 m/m.y.; Portenga and Bierman, 2011), and these rates are consistent with the extensive preservation of low-relief erosional surfaces throughout the Peninsular Ranges (Dorsey and Burns, 1994). Most importantly, even minimum denudation rates along the active escarpment (~70 m/m.y.) are an order of magnitude faster than summit denudation rates (<8 m/m.y.), making this surface an effective structural datum with which to constrain relief generation across the entire Sierra San Pedro Mártir escarpment. Within this conceptual framework, the modern elevation of the eastern edge of the Eocene erosion surface is interpreted to reflect accumulated footwall uplift relative to base level. River longitudinal profiles upstream of knickpoints are thought to reflect rock uplift rates relative to base level prior to an acceleration of uplift, while river longitudinal profiles downstream of knickpoints reflect modern rock uplift rates relative to base level (Fig. 3B). Consequently, relationships between river morphology and CRN_{DR} (section 6.1) can be used to calculate both recent increases in rock uplift rate relative to base level (section 6.2) and to estimate the age of initiation of the Sierra San Pedro Mártir normal faulting (section 6.3) as long as millennial-scale denudation rates are reflective of longer-term (10^5–10^6 yr) denudation rates.

6.1 Topography and Denudation Rates

The clear spatial correlation among position along the Sierra San Pedro Mártir fault system, geomorphic metrics, and CRN_{DR} *(*Fig. 5) indicates that tectonically driven rock uplift rates relative to base level have exerted the dominant control on catchment morphology and denudation rates. To better characterize this, we plotted catchment-averaged CRN_{DR} against catchment-averaged hillslope gradient (S_{avg}) and normalized channel steepness index (k_{sn}) in Figure 7. Removal of two anomalously high CRN_{DR} samples (MQ-07 and MQ-19, shown on plot) improves goodness of fit for catchment-averaged hillslope gradient (r^2 = 0.23 vs. r^2 = 0.52) and normalized channel steepness index (r^2 = 0.43 vs. r^2 = 0.66). However, these potential outliers do not substantially alter fit parameters and are thus included in reported regressions. Because there are measurement uncertainties in both x and y (especially for k_{sn} and CRN_{DR}), linear regressions shown in Figure 7 use a least squares estimation where uncertainties in both x and y are assumed to be uncorrelated (York et al., 2004).

Figure 7A shows the relationship between S_{avg} and CRN_{DR} in the Sierra San Pedro Mártir where the highest mean slopes are ~35°. Because the Sierra San Pedro Mártir bears the marks of a landscape where mass wasting processes dominate (i.e., patchy soils and large tracts of exposed bedrock), we expect that hillslope gradients are nearing thresholds set by material strength (Schmidt and Montgomery, 1995; Burbank et al., 1996; Hovius et al., 1998; Montgomery and Brandon, 2002; Larsen and Montgomery, 2012). As such, we plotted data alongside predictions of S_{avg} using a one-dimensional nonlinear colluvial transport model (dashed line) set to reasonable estimates of transport coefficient (K_h = 0.005 m^2/yr), slope threshold (S_c = 39°), and hillslope length (75 m; Roering et al., 2007). We also show the linear regression to these data (solid line). Assessing slope thresholds in this setting is challenging because, excluding one anomalously high sample (MQ-19), CRN_{DR} values in the Sierra San Pedro Mártir do not exceed 210 m/m.y. Prior studies have shown that thresholds in catchment-averaged hillslope gradient are not apparent until denudation rates exceed 200–300 m/m.y. (Binnie et al., 2007; DiBiase et al., 2010; Ouimet et al., 2009). As such, we can only conclude that the thresholds in catchment-averaged slope are ~35° or greater in the Sierra San Pedro Mártir.

Figure 7B shows the comparable relationship between channel steepness (k_{sn}) and CRN_{DR}. Like catchment-averaged hillslope gradient (S_{avg}), k_{sn} values show a robust linear relationship with CRN_{DR}. The fact that nested and replicate samples do not systematically deviate from the overall trend gives us confidence that the assumption of uniform mixing of alluvial sediments is valid for the Sierra San Pedro Mártir. The size of the data set and the corroboration of rates determined from two different laboratories also give us confidence that catchment-averaged channel steepness is faithfully recording the climatically and lithologically mediated response to tectonic forcing in the Sierra San Pedro Mártir. Although some previous studies have documented nonlinear relationships between channel steepness and denudation rates (Snyder et al., 2000; Duvall et al., 2004; Harkins et al., 2007; Ouimet et al., 2009; Cyr et al., 2010; DiBiase et al., 2010; Godard et al., 2014; Scherler et al., 2014), this does not appear to be the case for the Sierra San Pedro Mártir. This result may be due to the fact that the Sierra San Pedro Mártir is among the least erosionally efficient (i.e., exhibits high fluvial relief for a given erosion rate), tectonically active landscapes in the published literature (for a summary of comparable data sets, see Kirby and Whipple, 2012), on par with observations from the eastern margin of the Tibetan Plateau (Ouimet et al., 2009). In east Tibet, nonlinearities in the relationship between channel steepness and denudation rates were not evident until channel steepness values exceeded ~250–300 m$^{0.9}$. Given that the observed erosional efficiency for the Sierra San Pedro Mártir is similarly low (Fig. 7B), maximum rock uplift rates relative to base level may not be high enough to resolve between linear and nonlinear relationships in this setting. Consequently, we took a conservative approach in extrapolating from observations by using the best-fit linear model to infer denudation rates in unsampled catchments and above and below knickpoints (section 6.2). This is conservative in the sense that it will minimize extrapolated denudation rates and thus give us maximum ages of recent

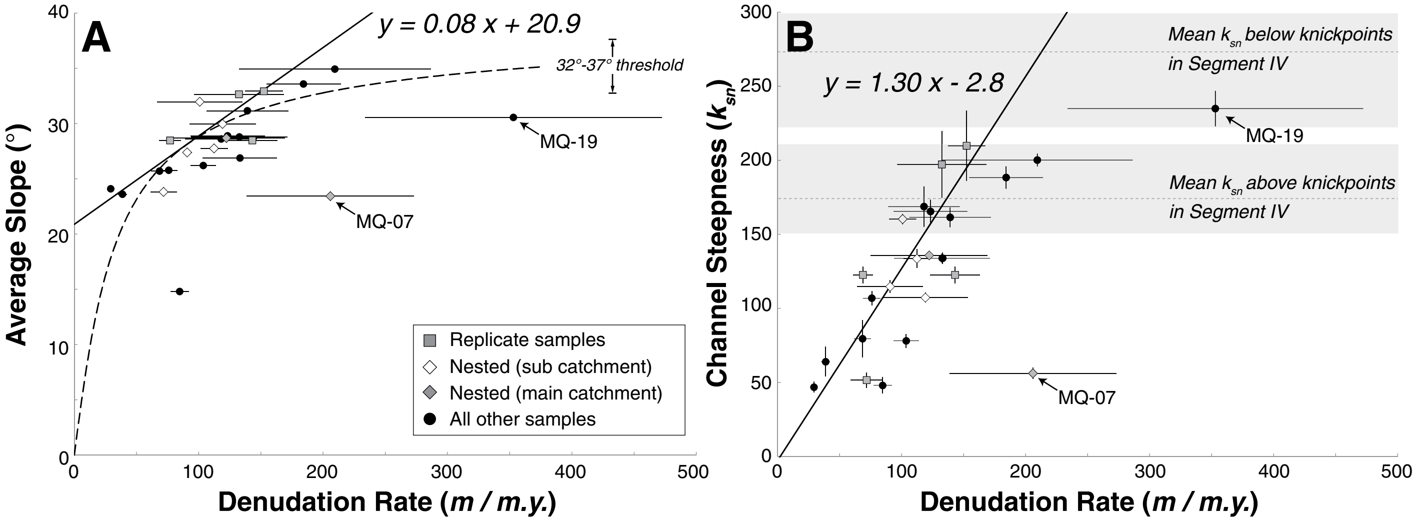

Figure 7. (A) Relationship between cosmogenic radionuclide–derived denudation rates (CRN_{DR}) and catchment-averaged slope angle and (B) relationship between CRN_{DR} and normalized channel steepness index for all catchments reported in Table 1 except MQ-08 (too small with a drainage area <0.2 km^2), where 1σ analytical uncertainties are shown for CRN_{DR}, and 2 standard errors about the mean are shown for slope and channel steepness. Coefficients of determination using simple linear regression for catchment-averaged slope (r^2 = 0.23) and channel steepness (r^2 = 0.43) dramatically increase when two potential outliers (MQ-07, MQ-19) are removed (r^2 = 0.52 for slope; r^2 = 0.66 for channel steepness). Because there are measurement uncertainties in both *x* and *y*, we used the approach of York et al. (2004) to determine the least-squares estimation for linear fits (solid lines). Replicate and nested samples are differentiated on plots but are each included in linear regressions. For A, predictions made from a nonlinear transport model (Eq. 2) are also shown as a reference (dashed line) and use a characteristic hillslope length of 75 m, *Sc* = 39°, and K = 0.005 m^2/yr (see equation 1 main text for description). For B, the range (gray shading) and mean (gray dashed line) of channel steepness values upstream and downstream of slope-break knickpoints in segment IV are shown for reference (*n* = 5). The linear relationship shown in B was used to predict denudation rates along strike in the Sierra San Pedro Mártir, ages of initiation of the Sierra San Pedro Mártir fault system, and the timing of recent increases in rock uplift rates as shown in Figure 8.

increases in rock uplift rates relative to base level and the onset of normal faulting in the Sierra San Pedro Mártir.

6.2 Late Pliocene Increase in Fault Slip Rates

Series of prominent slope-break knickpoints in channel profiles along segments II, III, and IV show a south to north increase in knickpoint elevation above base level (up to ~700 m; see Figs. 2 and 3). In general, this morphology could be caused by systematic along-strike variation in lithology, climate, or tectonics. Stationary lithologic knickpoints can form in the landscape if contacts are near vertical. Knickpoints in the Sierra San Pedro Mártir are not correlated with mapped geologic contacts and thus provide no evidence of a lithologic control. In contrast, if slope-break knickpoints are attributed to changes in rock uplift rates or persistent changes in climate (e.g., due to increasing aridity), then knickpoints are transient features that are generated as the landscape adjusts to a new forcing (Whipple and Tucker, 1999; Bonnet and Crave, 2003; Whittaker and Boulton, 2012). Stable isotope analysis of paleosols in southern California argue for a persistent increase in aridity during the Pliocene–Pleistocene (Peryam et al., 2011) that is roughly coincident with the inferred timing of the propagation of slope-break knickpoints in the Sierra San Pedro Mártir (see following). However, climatic forcing would not produce the steady south to north increase in slope-break knickpoint elevations observed in the Sierra San Pedro Mártir (Fig. 3A). Furthermore, neither lithologic nor climatic interpretations of knickpoints help to explain why accumulated rock uplift is skewed toward the north, as demonstrated by patterns in surface uplift of the Eocene erosional surface (Fig. 3A). As such, we strongly favor a tectonic origin for the slope-break knickpoints, albeit one that is nonuniform along strike. Slope-break knickpoints driven by increases in rock uplift rates relative to base level are now recognized in a large number of tectonically active settings (e.g., Schoenbohm et al., 2004; Clark et al., 2005; Dorsey and Roering, 2006; Harkins et al., 2007; Kirby et al., 2007; Miller et al., 2012, 2013; Schildgen et al., 2012; Whittaker and Boulton, 2012; Ellis et al., 2015). In these settings, denudation rates below the knickpoint are in balance with new uplift rates, and those above are in balance with old uplift rates and provide a geomorphic constraint to date increases in rock uplift rates relative to base level (Whipple and Tucker, 1999; Whittaker et al., 2008).

In the Sierra San Pedro Mártir, we estimated the timing of the increase in footwall rock uplift rates relative to base level by using the relationship between CRN_{DR} and channel steepness (k_{sn}) shown in Figure 7B, combined with estimates of k_{sn} upstream and downstream of prominent slope-break knickpoints (see Table DR2 [see footnote 1]). For the nine southernmost knickpoints, where the magnitude of upstream migration of knickpoints is small, back filling of channel reaches with alluvial sediment prevents reliable measurement of downstream values of k_{sn}. However, the five northernmost knickpoints (all in segment IV) have propagated the farthest upstream, and there is little evidence of substantial aggradation upstream of the outlets. As such, these channel reaches are long enough to make reasonable estimates of channel steepness. The mean channel steepness values upstream (k_{sn} = 174 ± 10) and downstream

(k_{sn} = 273 ± 18) of these knickpoints suggest a corresponding increase in denudation rates (136 ± 8 m/m.y. and 213 ± 14 m/m.y. above and below knickpoints, respectively) based on the regression shown in Figure 7B. By using the vertical difference in knickpoint and outlet elevations and estimates of denudation rates below knickpoints as a proxy for modern rock uplift rates relative to base level (Fig. 7B), we estimated maximum ages for the recent increase in footwall rock uplift rates relative to base level assuming that knickpoints propagated at a constant vertical velocity set by the new rock uplift rate (Eq. 4; Niemann et al., 2001). Using this approach, the mean age (n = 5) for the increase in rock uplift rates is 2.9 Ma, and calculations for individual catchments range from 1.9 Ma to 3.5 Ma. (Table DR2 [see footnote 1]). Because these slope-break knickpoints have propagated the farthest upstream, these watersheds provide an estimate of maximum rock uplift rates relative to base level, and their mean value provides the best age estimate for the recent increase in footwall rock uplift rates relative to base level. Surface uplift of a topographic bench (~200 m above the modern base level) near the transition between segments II and III (Fig. 6) provides an opportunity for future studies attempting to directly date the recent increase in rock uplift rates relative to base level in the Sierra San Pedro Mártir. However, before such dates can be useful, the source of discrepancies between the knickpoint elevation above base level (~400 m) and the elevation of the bench above base level (~200 m) must be determined (Fig. 6B).

6.3 Middle–Late Miocene Onset Age of Sierra San Pedro Mártir Faulting

Regional constraints provide a framework within which to evaluate how well millennial-scale denudation rates reported here compare to the longer-term rate of rock uplift relative to base level recorded in channel profiles (e.g., Kirby and Whipple, 2012). In the southern portion of the Sierra San Pedro Mártir, the ca. 12.6 Ma Tuff of San Felipe is offset and unconformably overlain by 6 Ma tuffs, thereby bracketing the onset of normal faulting between these ages (Stock and Hodges, 1989). North of the Sierra San Pedro Mártir, the onset of faulting in the Sierra Juarez has been dated between ca. 16 and 11 Ma using $^{40}Ar/^{39}Ar$ geochronology and was interpreted to precede faulting along the Main Gulf Escarpment (Lee et al., 1996). To the east, in the hanging wall of the Sierra San Pedro Mártir, the onset of faulting in the San Felipe fault array has been dated to ca. 9–8 Ma using stratigraphic relationships combined with $^{40}Ar/^{39}Ar$ geochronology, as well apatite fission-track and (U-Th)/He thermochronology (Seiler et al., 2011, 2013). However, few constraints exist for the onset of the Sierra San Pedro Mártir fault system itself.

If millennial-scale denudation rates provide a reasonable proxy for longer-term rock uplift rates relative to base level, then the CRN_{DR}-k_{sn} relationship can be combined with accumulated surface uplift of the Eocene erosional surface to estimate the onset age of Sierra San Pedro Mártir faulting (Table DR1 [see footnote 1]). While millennial-scale erosion rates may either under- or overestimate long-term rock uplift rates, patterns in relative ages are considered robust. Along-strike variations in the topography imply smooth variations in the relative timing of faulting, with segments III and IV showing clear evidence for a recent acceleration in rock uplift rates relative to base level. To calculate accumulated surface uplift relative to base level since faulting began, we used the difference between the elevation of the edge of the Eocene erosional surface and outlet elevation for each catchment (Fig. 8A). To standardize the approach, we projected the centroid of each watershed to the eastern edge of the Eocene erosional surface and determined the mean elevation of this edge over a 2 km window. Accumulated surface uplift was then interpreted to be the difference between the 2 km averaged elevation and its corresponding outlet elevation at the range front. Mean channel steepness (k_{sn}) values for each catchment were then used to calculate denudation rates using the CRN_{DR} - k_{sn} relationship reported in Figure 7B. Modeled denudation rates are shown in Figure 8B (dark gray line) and in Table DR1 (see footnote 1). Denudation rates from catchments that do not share a divide with the Eocene erosional surface are shown separately in Figure 8B (dark gray crosses) because they cannot be used to calculate onset ages for normal faulting, but they corroborate along-strike variations in inferred denudation rates. The along-strike variation in modern denudation rates shown in Figure 8B is more skewed than the elevations of the Eocene erosional surface (Fig. 8A). We

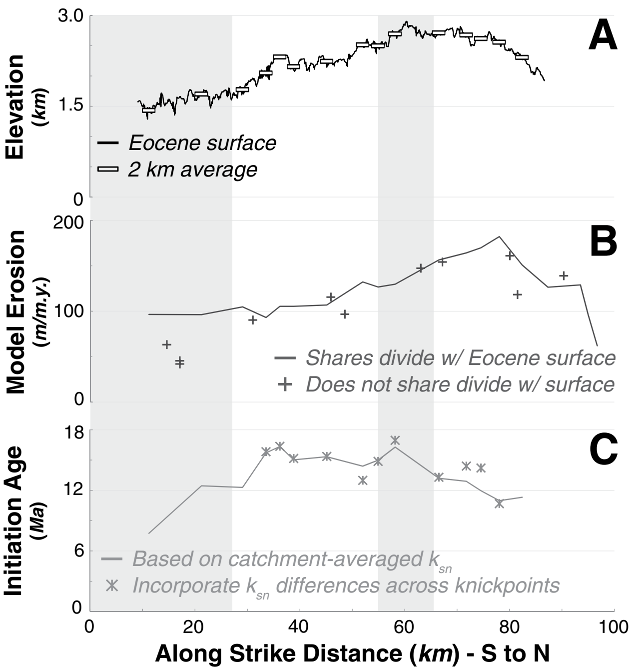

Figure 8. (A) Elevations of the eastern edge of the Eocene erosional surface replotted to show 2-km-radius average values for each catchment in the Sierra San Pedro Mártir. (B–C) By combining these data with model erosion rates determined from Figure 6B (B), we were able to determine the onset of normal faulting along strike in the Sierra San Pedro Mártir (C). Note that the Eocene erosional surface is not preserved past km 80–85 in A, and thus fault initiation cannot be inferred beyond this point. In B, the regression-based denudation rates are shown for catchments that share a divide with the Eocene erosional surface versus those that do not. In C, initiation ages implied by two-staged uplift of the surface (i.e., those catchments with slope-break knickpoints) are also shown. Morphometrics used to calculate two-stage uplift model are reported in Table DR2 (see text footnote 1).

interpret the increased skewness to be a direct reflection of increased rock uplift rates relative to base level in the northern segments during the late Pliocene (see section 6.2). Finally, Figure 8C shows the result of dividing the accumulated surface uplift (Fig. 8A) by the inferred rate of rock uplift relative to base level (Fig. 8B) and thus provides maximum age estimates for the onset of normal faulting in the Sierra San Pedro Mártir (light gray line). Figure 8C also shows onset ages for two-staged models of uplift relative to base level, where denudation rates are treated separately upstream and downstream of slope-break knickpoints (light gray asterisks). Two-stage models of uplift relative to base level do not substantially affect predictions of the initiation age.

There are several basic observations that can be made from this analysis and Figure 8. First, while recent increases in rock uplift rates relative to base level in the north are important to explain the asymmetric pattern in surface uplift, ages of onset using a single, average uplift rate are not substantially different from those derived using a two-staged uplift calculation. This is because the k_{sn} - CRN_{DR} relationship is linear, which leads to a simple averaging between upstream and downstream differences in channel steepness and denudation rate. In other settings, where nonlinear k_{sn} - CRN_{DR} relationships exist, larger differences between multistage uplift histories would be expected. Second, our calculation of maximum ages for the onset of normal faulting in the Sierra San Pedro Mártir initiated ca. 16–14 Ma in fault segments II and III and ca. 12–8 Ma in segments I and IV (Fig. 8C). Uncertainties in the absolute values of fault-onset age estimates relate to how faithfully CRN_{DR} estimates represent longer-term rock uplift rates relative to base level and how well the CRN_{DR}-k_{sn} relationship captures spatial and temporal variations (see discussion in section 6.1).

Differences in onset ages for fault initiation on different fault segments that have since merged to define the Sierra San Pedro Mártir fault system favor the hypothesis that growth of the Sierra San Pedro Mártir fault system occurred via progressive linkage of initially distinct segments (e.g., Cartwright et al., 1995), with possible lateral propagation of fault tips to form segments I and IV at a later time. The most rapid CRN_{DR} rates and highest relief occur at the intersection of segments III and IV (rather than in the middle of individual segments), implying that the four Sierra San Pedro Mártir fault segments currently behave as a kinematically linked rupture system. On this basis, the arcuate, segmented geomorphic expression of the Sierra San Pedro Mártir fault trace and length of individual segments are interpreted as relict structural features (Fig. 2C) that no longer exert a fundamental control on the development of footwall topography and relief. It is important to emphasize that findings from our analysis of footwall topography do not imply that total finite slip is uncorrelated with fault segment boundaries. Determining the slip budget requires the inclusion of hanging-wall subsidence, and large gradients in finite slip are definitively correlated with segment boundaries (Seiler et al., 2010). Gradients are instead manifested by the clockwise rotation of hanging-wall blocks of the Sierra San Felipe (Fig. 2B), where each rotated block is associated with each fault segment (Seiler et al.. 2010).

6.4 Tectonic Implications

Our calculations indicate an initiation of Sierra San Pedro Mártir faulting that is on the high end of regional estimates (ca. 16–14 Ma), but possibly concurrent with the initiation of faulting in the Sierra Juarez (ca. 16–11 Ma). The offset Tuff of San Felipe (ca. 12.6 Ma) places a firm maximum bound, and the deposition of ca. 6 Ma tuffs that are not offset places a minimum bound on the initiation of normal faulting in the southern portion of segment I (Stock and Hodges, 1990). Initiation ages determined from our geomorphic analysis of the three southernmost catchments are consistent with these bounds (ca. 12–8 Ma) and thus give us confidence that millennial-scale denudation rates are representative of longer-term exhumation rates.

The proposed late Pliocene increase in footwall rock uplift rates in the Sierra San Pedro Mártir coincides with the waning and cessation of slip across several detachment faults located in the Sierra San Felipe to the east, based on a shoaling of rift basin sedimentation and progradation of late Pliocene–Pleistocene alluvial fans over lacustrine and shallow-marine sediments (Seiler et al., 2013). As described by Seiler et al. (2010), faults in the Sierra San Felipe have a listric geometry, and those in the north accommodate more extension than those in the south. The northward-increasing strain gradient would also translate to a northward increase in fault slip on the Sierra San Pedro Mártir once hanging-wall faults were abandoned. It is therefore possible that the late Pliocene increase in rock uplift rates relative to base level along the Sierra San Pedro Mártir fault system occurred due to a transfer of extensional strain from detachment faults east of the Sierra San Pedro Mártir.

At the regional scale, the Sierra San Pedro Mártir fault system and detachments in the Sierra San Felipe form the basal strands of a midcrustal detachment system that was the dominant structure accommodating opening of this section of the northern Gulf of California (Martín-Barajas et al., 2013). Seismic profiles offshore show that parts of this detachment system were abandoned in the Pliocene when oblique rifting localized in the Delfin basins, and ultimately led to continental lithospheric rupture and the emplacement of ~35 km of new oceanic crust (Martín-Barajas et al., 2013). Our analysis strongly suggests that the Sierra San Pedro Mártir fault, which forms the breakaway strand of the detachment system, did not die with the rest of the detachment faults in its hanging wall. Rather, slip on the Sierra San Pedro Mártir appears to have accelerated during the Pliocene reorganization of plate margin shearing that led to the localization of extension in the Delfin basins. Three main factors likely contributed to prevent cessation of Sierra San Pedro Mártir faulting during this time. First, while most of the detachment system is associated with low elevations near or below sea level, the high gravitational potential energy gradient of the escarpment itself is a major driver that can explain continued activity on the Sierra San Pedro Mártir fault system. Second, the Pliocene reorganization of the plate margin can be described as a westward migration of shearing (Aragón-Arreola and Martín-Barajas, 2007). While drivers for this migration are not fully understood, recent work suggests that strain relocation may be an inherent process during the formation of hyperextended, asymmetric margins (Brune et al., 2014). In the case of the Gulf of California, the locus of extension relocated closer toward the trailing edge of the Baja California microplate (e.g., Fletcher et al., 2007), forming a new system of extensional basins and transfer faults in the western gulf region that eventually resulted in continental rupture (Aragón-Arreola and Martín-Barajas, 2007; Martín-Barajas et al., 2013). The Sierra San Pedro Mártir fault system defines the western boundary of extension and is in the immediate vicinity of the applied tectonic stress of the relocated plate boundary, some 80–100 km further east. Third, the Sierra San Pedro Mártir fault system dips steeply to the east and is optimally oriented to accommodate extension. The magnitude of critical differential stress is therefore more favorable here than in the shallowly dipping detachments to the east. Regardless of whether this late Pliocene event was controlled by regional geodynamics or represents a more local transfer of strain, our analysis demonstrates that detailed inspection of fluvial channel profiles along with CRN_{DR} analysis can provide important insights into the tectonic and structural evolution of a mountain range.

7. CONCLUSIONS

We present a suite of new ^{10}Be-derived denudation rates along an uplifted footwall of a major normal fault in the Gulf Extensional Province. Consistent with theory and other field studies where climate and lithology are held constant, denudation rates in the Sierra San Pedro Mártir are strongly correlated with topographic relief. Catchment-averaged hillslope gradient, 2.5-km-radius local relief, and channel steepness each covary with accumulated footwall uplift as expressed by the modern elevations of an Eocene erosional surface. Denudation rates on this surface are very slow (<10 m/m.y.) compared to the active escarpment (maximum rates >200 m/m.y.; mean rates >100 m/m.y.). Asymmetry in surface uplift of this erosional surface was likely driven by a late Pliocene (ca. 3–2 Ma) increase in footwall rock uplift rates relative to base level that is expressed in the topography as a series of slope-break knickpoints of increasing elevation toward the north. Recent increases in rock uplift rates could be due to a transfer of strain associated with the demise of hanging-wall detachments to the east and/or reflect the regional reorganization of plate margin shearing during the Pliocene. Relationships between millennial-scale denudation rates and normalized channel steepness suggest a maximum age of initiation for the Sierra San Pedro Mártir fault system of ca. 16–14 Ma in the central portion of the range. Onset ages are younger in northern (IV) and southern (I) segments (ca. 12–8 Ma) and are consistent with independent regional constraints for the onset of normal faulting. We hypothesize that the Sierra San Pedro Mártir fault system initiated as kinematically distinct faults in the Miocene, leading to the highly segmented geomorphic expression of the Sierra San Pedro Mártir range front. These faults eventually became linked into the modern system via segment linkage. This study shows how careful pairing of CRN_{DR} with topographic analysis can be used to reveal the pace and pattern of deformation over geologic time scales.

ACKNOWLEDGMENT

We want to thank A. Duvall, M. Ellis, and the Associate Editor K. Wegmann for thoughtful reviews that improved the quality of this manuscript. This work was supported by funding from the Geomorphology and Landuse Dynamics Program at National Science Foundation (EAR-0921705 to KXW).

REFERENCES CITED

Adams, B.A., Whipple, K.X., Hodges, K.V., and Heimsath, A.M., 2016, In-situ development of high-elevation, low-relief landscapes via duplex deformation in the Eastern Himalayan hinterland, Bhutan: Journal of Geophysical Research–Earth Surface, v. 121, no. 2, p. 294–319, doi:10.1002/2015JF003508.

Ahnert, F., 1970, Functional relationships between denudation, relief, and uplift in large mid-latitude drainage basins: American Journal of Science, v. 268, no. 3, p. 243–263, doi:10.2475/ajs.268.3.243.

Anderson, R.S., and Anderson, S.P., 2010, Geomorphology: The Mechanics and Chemistry of Landscapes: Cambridge, UK, Cambridge University Press, 651 p., doi:10.1017/CBO9780511794827.

Aragón-Arreola, M., and Martín-Barajas, A., 2007, Westward migration of extension in the northern Gulf of California, Mexico: Geology, v. 35, no. 6, p. 571–574, doi:10.1130/G23360A.1.

Atwater, T., and Stock, J., 1998, Pacific–North America plate tectonics of the Neogene southwestern United States: An update: International Geology Review, v. 40, no. 5, p. 375–402, doi:10.1080/00206819809465216.

Axen, G., 1995, Extensional segmentation of the main Gulf escarpment, Mexico and United States: Geology, v. 23, no. 6, p. 515–518, doi:10.1130/0091-7613(1995)023<0515:ESOTMG>2.3.CO;2.

Axen, G.J., and Fletcher, J.M., 1998, Late Miocene-Pleistocene extensional faulting, northern Gulf of California, Mexico and Salton Trough, California: International Geology Review, v. 40, no. 3, p. 217–244.

Axen, G.J., Grove, M., Stockli, D., Lovera, O.M., Rothstein, D.A., Fletcher, J.M., Farley, K., and Abbott, P.L., 2000, Thermal evolution of Monte Blanco dome: Low-angle normal faulting during Gulf of California rifting and late Eocene denudation of the eastern Peninsular Ranges: Tectonics, v. 19, no. 2, p. 197–212, doi:10.1029/1999TC001123.

Balco, G., Stone, J.O., Lifton, N.A., and Dunai, T.J., 2008, A complete and easily accessible means of calculating surface exposure ages or erosion rates from (10)Be and (26)Al measurements: Quaternary Geochronology, v. 3, no. 3, p. 174–195, doi:10.1016/j.quageo.2007.12.001.

Berlin, M.M., and Anderson, R.S., 2007, Modeling of knickpoint retreat on the Roan Plateau, western Colorado: Journal of Geophysical Research–Earth Surface (2003–2012), v. 112, no. F3, p. F03S06, doi:10.1029/2006JF000553.

Bierman, P., and Steig, E.J., 1996, Estimating rates of denudation using cosmogenic isotope abundances in sediment: Earth Surface Processes and Landforms, v. 21, no. 2, p. 125–139, doi:10.1002/(SICI)1096-9837(199602)21:2<125::AID-ESP511>3.0.CO;2-8.

Binnie, S.A., Phillips, W.M., Summerfield, M.A., and Fifield, L.K., 2007, Tectonic uplift, threshold hillslopes, and denudation rates in a developing mountain range: Geology, v. 35, no. 8, p. 743–746, doi:10.1130/G23641A.1.

Bonnet, S., and Crave, A., 2003, Landscape response to climate change: Insights from experimental modeling and implications for tectonic versus climatic uplift of topography: Geology, v. 31, no. 2, p. 123–126, doi:10.1130/0091-7613(2003)031<0123:LRTCCI>2.0.CO;2.

Brown, L.G., 1978, Recent Fault Scarps along the Eastern Escarpment of the Sierra San Pedro Mártir, Baja, California [M.S. thesis]: San Diego, California, San Diego State University, 108 p.

Brune, S., Heine, C., Perez-Gussinye, M., and Sobolev, S.V., 2014, Rift migration explains continental margin asymmetry and crustal hyper-extension: Nature Communications, v. 5, 4014, doi:10.1038/ncomms5014.

Burbank, D.W., Leland, J., Fielding, E., Anderson, R.S., Brozovic, N., Reid, M.R., and Duncan, C., 1996, Bedrock incision, rock uplift and threshold hillslopes in the northwestern Himalayas: Nature, v. 379, no. 6565, p. 505–510, doi:10.1038/379505a0.

Cartwright, J.A., Trudgill, B.D., and Mansfield, C.S., 1995, Fault growth by segment linkage: An explanation for scatter in maximum displacement and trace length data from the Canyonlands grabens of SE Utah: Journal of Structural Geology, v. 17, no. 9, p. 1319–1326, doi:10.1016/0191-8141(95)00033-A.

Clark, M.K., Maheo, G., Saleeby, J., and Farley, K.A., 2005, The non-equilibrium landscape of the southern Sierra Nevada, California: GSA Today, v. 15, no. 9, p. 4–10, doi:10.1130/1052-5173(2005)015[4:TNLOTS]2.0.CO;2.

Cowie, P.A., and Scholz, C.H., 1992, Displacement-length scaling relationship for faults: Data synthesis and discussion: Journal of Structural Geology, v. 14, no. 10, p. 1149–1156, doi:10.1016/0191-8141(92)90066-6.

Crosby, B.T., and Whipple, K.X, 2006, Knickpoint initiation and distribution within fluvial networks: 236 waterfalls in the Waipaoa River, North Island, New Zealand: Geomorphology, v. 82, no. 1, p. 16–38.

Cyr, A.J., and Granger, D.E., 2008, Dynamic equilibrium among erosion, river incision, and coastal uplift in the northern and central Apennines, Italy: Geology, v. 36, no. 2, p. 103–106, doi:10.1130/G24003A.1.

Cyr, A.J., Granger, D.E., Olivetti, V., and Molin, P., 2010, Quantifying rock uplift rates using channel steepness and cosmogenic nuclide–determined erosion rates: Examples from northern and southern Italy: Lithosphere, v. 2, no. 3, p. 188–198, doi:10.1130/L96.1.

Dawers, N.H., and Anders, M.H., 1995, Displacement-length scaling and fault linkage: Journal of Structural Geology, v. 17, no. 5, p. 607–614, doi:10.1016/0191-8141(94)00091-D.

Dawers, N.H., Anders, M.H., and Scholz, C.H., 1993, Growth of normal faults: Displacement-length scaling: Geology, v. 21, no. 12, p. 1107–1110, doi:10.1130/0091-7613(1993)021<1107:GONFDL>2.3.CO;2.

Densmore, A.L., Hetzel, R., Ivy-Ochs, S., Krugh, W.C., Dawers, N., and Kubik, P., 2009, Spatial variations in catchment-averaged denudation rates from normal fault footwalls: Geology, v. 37, no. 12, p. 1139–1142, doi:10.1130/G30164A.1.

DiBiase, R.A., and Whipple, K.X., 2011, The influence of erosion thresholds and runoff variability on the relationships among topography, climate, and erosion rate: Journal of Geophysical Research–Earth Surface, v. 116, p. F04036, *doi:*10.1029/2011JF002095.

DiBiase, R.A., Whipple, K.X., Heimsath, A.M., and Ouimet, W.B., 2010, Landscape form and millennial erosion rates in the San Gabriel Mountains, CA: Earth and Planetary Science Letters, v. 289, no. 1–2, p. 134–144, doi:10.1016/j.epsl.2009.10.036.

Dorsey, R.J., and Burns, B., 1994, Regional stratigraphy, sedimentology, and tectonic significance of Oligocene–Miocene sedimentary and volcanic rocks, northern Baja California, Mexico: Sedimentary Geology, v. 88, no. 3–4, p. 231–251, doi:10.1016/0037-0738(94)90064-7.

Dorsey, R.J., and Roering, J.J., 2006, Quaternary landscape evolution in the San Jacinto fault zone, Peninsular Ranges of Southern California: Transient response to strike-slip fault initiation: Geomorphology, v. 73, no. 1–2, p. 16–32, doi:10.1016/j.geomorph.2005.06.013.

Duvall, A., Kirby, E., and Burbank, D., 2004, Tectonic and lithologic controls on bedrock channel profiles and processes in coastal California: Journal of Geophysical Research–Earth Surface, v. 109, no. F3, p. F03002, doi:10.1029/2003JF000086.

Ellis, M.A., Barnes, J.B., and Colgan, J.P., 2015, Geomorphic evidence for enhanced Pliocene–Quaternary faulting in the northwestern Basin and Range: Lithosphere, v. 7, no. 1, p. 59–72, doi:10.1130/L401.1.

Farr, T.G., Rosen, P.A., Caro, E., Crippen, R., Duren, R., Hensley, S., Kobrick, M., Paller, M., Rodriguez, E., Roth, L., Seal, D., Shaffer, S., Shimada, J., Umland, J., Werner, M., Oskin, M., Burbank, D., and Alsdorf, D., 2007, The Shuttle Radar Topography Mission: Reviews of Geophysics, v. 45, no. 2, doi:10.1029/2005RG000183.

Fenby, S.S., and Gastil, R.G., 1991, Geologic-tectonic map of the Gulf of California and surrounding areas: The Gulf and Peninsular Province of the Californias: American Association of Petroleum Geologists Memoir, v. 47, p. 79–83.

Fletcher, J.M., Grove, M., Kimbrough, D.L., Lovera, O., and Gehrels, G.E., 2007, Ridge-trench interactions and the Neogene tectonic evolution of the Magdalena shelf and southern Gulf of California: Insights from detrital zircon U-Pb ages from the Magdalena fan and adjacent areas: Geological Society of America Bulletin, v. 119, no. 11–12, p. 1313–1336, doi:10.1130/B26067.1.

Flint, J.J., 1974, Stream gradient as a function of order, magnitude, and discharge: Water Resources Research, v. 10, no. 5, p. 969–973, doi:10.1029/WR010i005p00969.

Gasparini, N.M., and Brandon, M.T., 2011, A generalized power law approximation for fluvial incision of bedrock channels: Journal of Geophysical Research–Earth Surface, v. 116, p. F02020, doi:10.1029/2009JF001655.

Gastelum, R.C., Romo, T.R., and Rabago, P.Y.H., 2000, Carta Geologico-Minera Lazaro, Cardenas: Servicio Geologico Mexicano.

Gastil, R.G., 1961, The elevated erosion surfaces, *in* Thomas, B.E., ed., Geological Society of America 57th Annual Meeting Guidebook for Field Trips: New York, Geological Society of America, Cordilleran Section, p. 1–4.

Gastil, R.G., Phillips, R.P., and Allison, E.C., 1975, Reconnaissance Geology of the State of Baja California: Geological Society of America Memoir 140, 170 p., doi:10.1130/MEM140-p1.

Gilbert, G.K., and Dutton, C.E., 1880, Report on the Geology of the Henry Mountains: Washington, D.C., U.S. Government Printing Office, 160 p.

Gleadow, A.J.W., Kohn, B.P., Fletcher, J.M., Brown, R.W., and Raza, A., 2003, Low-temperature thermochronology of fundamental structures in the Gulf Extensional Province, Baja California, Mexico: Geochimica et Cosmochimica Acta, v. 67, no. 18, p. A122–A122.

Godard, V., Bourlès, D.L., Spinabella, F., Burbank, D.W., Bookhagen, B., Fisher, G.B., Moulin, A., and Léanni, L., 2014, Dominance of tectonics over climate in Himalayan denudation: Geology, v. 42, no. 3, p. 243–246.

Granger, D.E., Kirchner, J.W., and Finkel, R., 1996, Spatially averaged long-term erosion rates measured from in situ–produced cosmogenic nuclides in alluvial sediment: The Journal of Geology, v. 104, no. 3, p. 249–257, doi:10.1086/629823.

Hack, J.T., 1957, Studies of Longitudinal Stream Profiles in Virginia and Maryland: U.S. Geological Survey Professional Paper 294-B, 97 p.

Hack, J.T., 1975, Dynamic equilibrium and landscape evolution, *in* Melhorn, W.N., and Flemal, R.C., eds., Theories of Landform Development: New York, State University of New York, p. 87–102.

Harkins, N., Kirby, E., Heimsath, A., Robinson, R., and Reiser, U., 2007, Transient fluvial incision in the headwaters of the Yellow River, northeastern Tibet, China: Journal of Geophysical Research–Earth Surface, v. 112, no. F3, p. F03S04, doi:10.1029/2006JF000570.

Hovius, N., Stark, C.P., and Allen, P.A., 1997, Sediment flux from a mountain belt derived by landslide mapping: Geology, v. 25, no. 3, p. 231–234, doi:10.1130/0091-7613(1997)025<0231:SFFAMB>2.3.CO;2.

Hovius, N., Stark, C.P., Tutton, M.A., and Abbott, L.D., 1998, Landslide-driven drainage network evolution in a pre-steady-state mountain belt: Finisterre Mountains, Papua New Guinea: Geology, v. 26, no. 12, p. 1071–1074, doi:10.1130/0091-7613(1998)026<1071:LDDNEI>2.3.CO;2.

Kirby, E., and Whipple, K., 2001, Quantifying differential rock-uplift rates via stream profile analysis: Geology, v. 29, no. 5, p. 415–418, doi:10.1130/0091-7613(2001)029<0415:QDRURV>2.0.CO;2.

Kirby, E., and Whipple, K.X., 2012, Expression of active tectonics in erosional landscapes: Journal of Structural Geology, v. 44, p. 54–75, doi:10.1016/j.jsg.2012.07.009.

Kirby, E., Johnson, C., Furlong, K., and Heimsath, A., 2007, Transient channel incision along Bolinas Ridge, California: Evidence for differential rock uplift adjacent to the San Andreas fault: Journal of Geophysical Research–Earth Surface, v. 112, no. F3, p. F03S07, doi:10.1029/2006JF000559.

Kohl, C.P., and Nishiizumi, K., 1992, Chemical isolation of quartz for measurement of in situ–produced cosmogenic nuclides: Geochimica et Cosmochimica Acta, v. 56, no. 9, p. 3583–3587, doi:10.1016/0016-7037(92)90401-4.

Lague, D., and Davy, P., 2003, Constraints on the long-term colluvial erosion law by analyzing slope-area relationships at various tectonic uplift rates in the Siwaliks Hills (Nepal): Journal of Geophysical Research–Solid Earth, v. 108, no. B2, p. 2129, doi:10.1029/2002JB001893.

Lague, D., Hovius, N., and Davy, P., 2005, Discharge, discharge variability, and the bedrock channel profile: Journal of Geophysical Research–Earth Surface, v. 110, no. F4, p. F04006, doi:10.1029/2004JF000259.

Lal, D., 1991, Cosmic ray labeling of erosion surfaces: in situ nuclide production rates and erosion models: Earth and Planetary Science Letters, v. 104, no. 2-4, p. 424–439.

Larsen, I.J., and Montgomery, D.R., 2012, Landslide erosion coupled to tectonics and river incision: Nature Geoscience, v. 5, no. 7, p. 468–473, doi:10.1038/ngeo1479.

Lee, J., Miller, M.M., Crippen, R., Hacker, B., and Vazquez, J.L., 1996, Middle Miocene extension in the Gulf Extensional Province, Baja California: Evidence from the southern Sierra Juarez: Geological Society of America Bulletin, v. 108, no. 5, p. 505–525, doi:10.1130/0016-7606(1996)108<0505:MMEITG>2.3.CO;2.

Martín-Barajas, A., Gonzalez-Escobar, M., Fletcher, J.M., Pacheco, M., Oskin, M., and Dorsey, R., 2013, Thick deltaic sedimentation and detachment faulting delay the onset of continental rupture in the northern Gulf of California: Analysis of seismic reflection profiles: Tectonics, v. 32, no. 5, p. 1294–1311, doi:10.1002/tect.20063.

Miller, S.R., Baldwin, S.L., and Fitzgerald, P.G., 2012, Transient fluvial incision and active surface uplift in the Woodlark Rift of eastern Papua New Guinea: Lithosphere, v. 4, no. 2, p. 131–149, doi:10.1130/L135.1.

Miller, S.R., Sak, P.B., Kirby, E., and Bierman, P.R., 2013, Neogene rejuvenation of Central Appalachian topography: Evidence for differential rock uplift from stream profiles and erosion rates: Earth and Planetary Science Letters, v. 369–370, p. 1–12, doi:10.1016/j.epsl.2013.04.007.

Montgomery, D.R., and Brandon, M.T., 2002, Topographic controls on erosion rates in tectonically active mountain ranges: Earth and Planetary Science Letters, v. 201, no. 3–4, p. 481–489, doi:10.1016/S0012-821X(02)00725-2.

Niemann, J.D., Gasparini, N.M., Tucker, G.E., and Bras, R.L., 2001, A quantitative evaluation of Playfair's law and its use in testing long-term stream erosion models: Earth Surface Processes and Landforms, v. 26, no. 12, p. 1317–1332, doi:10.1002/esp.272.

Niemi, N.A., Oskin, M., Burbank, D.W., Heimsath, A.M., and Gabet, E.J., 2005, Effects of bedrock landslides on cosmogenically determined erosion rates: Earth and Planetary Science Letters, v. 237, no. 3–4, p. 480–498, doi:10.1016/j.epsl.2005.07.009.

O'Connor, J.E., and Chase, C.G., 1989, Uplift of the Sierra San Pedro Martir, Baja California, Mexico: Tectonics, v. 8, no. 4, p. 833–844, doi:10.1029/TC008i004p00833.

Olivetti, V., Cyr, A.J., Molin, P., Faccenna, C., and Granger, D.E., 2012, Uplift history of the Sila Massif, southern Italy, deciphered from cosmogenic Be-10 erosion rates and river longitudinal profile analysis: Tectonics, v. 31, p. TC3007, doi:10.1029/2011TC003037.

Ortega-Rivera, A., 2003, Geochronological constraints on the tectonic history of the Peninsular Ranges batholith of Alta and Baja California: Tectonic implications for western Mexico, *in* Johnson, S.E., Paterson S.R., Fletcher J.M., Girty, G.H., Kimbrough, D.L., and Martín-Barajas, A., eds., Tectonic Evolution of Northwestern Mexico and the Southwestern USA: Geological Society of America Special Paper 374, p. 297–336.

Ouimet, W.B., Whipple, K.X., and Granger, D.E., 2009, Beyond threshold hillslopes: Channel adjustment to base-level fall in tectonically active mountain ranges: Geology, v. 37, no. 7, p. 579–582, doi:10.1130/G30013A.1.

Penck, W., 1953, Morphological Analysis of Land Forms: A Contribution to Physical Geography: London, Macmillan and Co., 429 p.

Peryam, T.C., Dorsey, R.J., and Bindeman, I., 2011, Plio-Pleistocene climate change and timing of Peninsular Ranges uplift in southern California: Evidence from paleosols and stable isotopes in the Fish Creek–Vallecito basin: Palaeogeography, Palaeoclimatology, Palaeoecology, v. 305, no. 1–4, p. 65–74, doi:10.1016/j.palaeo.2011.02.014.

Portenga, E.W., and Bierman, P.R., 2011, Understanding Earth's eroding surface with ^{10}Be: GSA Today, v. 21, no. 8, p. 4–10, doi:10.1130/G111A.1.

Quigley, M., Sandiford, M., Fifield, L.K., and Alimanovic, A., 2007, Landscape responses to intraplate tectonism: Quantitative constraints from Be-10 nuclide abundances: Earth and Planetary Science Letters, v. 261, no. 1–2, p. 120–133, doi:10.1016/j.epsl.2007.06.020.

Roering, J.J., Kirchner, J.W., and Dietrich, W.E., 1999, Evidence for nonlinear, diffusive sediment transport on hillslopes and implications for landscape morphology: Water Resources Research, v. 35, no. 3, p. 853–870, doi:10.1029/1998WR900090.

Roering, J.J., Perron, J.T., and Kirchner, J.W., 2007, Functional relationships between denudation and hillslope form and relief: Earth and Planetary Science Letters, v. 264, no. 1–2, p. 245–258, doi:10.1016/j.epsl.2007.09.035.

Rosenbloom, N.A., and Anderson, R.S., 1994, Hillslope and channel evolution in a marine terraced landscape, Santa Cruz, California: Journal of Geophysical Research–Solid Earth, v. 99, no. B7, p. 14,013–14,029, doi:10.1029/94JB00048.

Safran, E.B., Bierman, P.R., Aalto, R., Dunne, T., Whipple, K.X., and Caffee, M., 2005, Erosion rates driven by channel network incision in the Bolivian Andes: Earth Surface Processes and Landforms, v. 30, no. 8, p. 1007–1024, doi:10.1002/esp.1259.

Scherler, D., Bookhagen, B., and Strecker, M. R., 2014, Tectonic control on ^{10}Be-derived erosion rates in the Garhwal Himalaya, India: Journal of Geophysical Research–Earth Surface, v. 119, no. 2, p. 83–105.

Schildgen, T.F., Cosentino, D., Bookhagen, B., Niedermann, S., Yildirim, C., Echtler, H., Wittmann, H., and Strecker, M.R., 2012, Multi-phased uplift of the southern margin of the Central Anatolian plateau, Turkey: A record of tectonic and upper mantle processes: Earth and Planetary Science Letters, v. 317–318, p. 85–95, doi:10.1016/j.epsl.2011.12.003.

Schmidt, K.L., Paterson, S.R., Blythe, A.E., and Kopf, C., 2009, Mountain building across a lithospheric boundary during arc construction: The Cretaceous Peninsular Ranges batholith in the Sierra San Pedro Martir of Baja California, Mexico: Tectonophysics, v. 477, no. 3–4, p. 292–310, doi:10.1016/j.tecto.2009.04.020.

Schmidt, K.M., and Montgomery, D.R., 1995, Limits to relief: Science, v. 270, no. 5236, p. 617–620, doi:10.1126/science.270.5236.617.

Schoenbohm, L.M., Whipple, K.X., Burchfiel, B.C., and Chen, L., 2004, Geomorphic constraints on surface uplift, exhumation, and plateau growth in the Red River region, Yunnan Province, China: Geological Society of America Bulletin, v. 116, no. 7–8, p. 895–909, doi:10.1130/B25364.1.

Seiler, C., 2009, Structural and Thermal Evolution of the Gulf Extensional Province in Baja California, Mexico: Implications for Neogene Rifting and Opening of the Gulf of California [Ph.D. thesis]: Melbourne, Australia, University of Melbourne, 307 p.

Seiler, C., Fletcher, J.M., Quigley, M.C., Gleadow, A.J.W., and Kohn, B.P., 2010, Neogene structural evolution of the Sierra San Felipe, Baja California: Evidence for proto-gulf transtension in the Gulf Extensional Province?: Tectonophysics, v. 488, no. 1–4, p. 87–109, doi:10.1016/j.tecto.2009.09.026.

Seiler, C., Fletcher, J.M., Kohn, B.P., Gleadow, A.J.W., and Raza, A., 2011, Low-temperature thermochronology of northern Baja California, Mexico: Decoupled slip-exhumation gradients and delayed onset of oblique rifting across the Gulf of California: Tectonics, v. 30, p. TC3004, doi:10.1029/2009TC002649.

Seiler, C., Quigley, M.C., Fletcher, J.M., Phillips, D., Gleadow, A.J.W., and Kohn, B.P., 2013, Stratigraphy and Ar-40/Ar-39 geochronology of the Santa Rosa basin, Baja California: Dynamic evolution of a constrictional rift basin during oblique extension in the Gulf of California: Basin Research, v. 25, no. 4, p. 388–418, doi:10.1111/bre.12004.

Silver, L., Allen, C., and Stehli, F., 1969, Geological and geochronological observations on a portion of the Peninsular Ranges batholith of northwestern Baja California, Mexico, *in* Abstracts for 1968: Abstracts of Papers Submitted for Seven Meetings with which the Society was Associated: Geological Society of America Special Paper 121, p. 279–280.

Sklar, L.S., and Dietrich, W.E., 2004, A mechanistic model for river incision into bedrock by saltating bed load: Water Resources Research, v. 40, no. 6.

Snyder, N.P., Whipple, K.X., Tucker, G.E., and Merritts, D.J., 2000, Landscape response to tectonic forcing: Digital elevation model analysis of stream profiles in the Mendocino triple junction region, northern California: Geological Society of America Bulletin, v. 112, no. 8, p. 1250–1263, doi:10.1130/0016-7606(2000)112<1250:LRTTFD>2.0.CO;2.

Spotila, J.A., Farley, K.A., and Sieh, K., 1998, Uplift and erosion of the San Bernardino Mountains associated with transpression along the San Andreas fault, California, as constrained by radiogenic helium thermochronometry: Tectonics, v. 17, no. 3, p. 360–378, doi:10.1029/98TC00378.

Stock, J.M., and Hodges, K.V., 1989, Pre-Pliocene extension around the Gulf of California and the transfer of Baja California to the Pacific plate: Tectonics, v. 8, no. 1, p. 99–115, doi:10.1029/TC008i001p00099.

Stock, J.M., and Hodges, K.V., 1990, Miocene to Recent structural development of an extensional accommodation zone, northeastern Baja California, Mexico: Journal of Structural Geology, v. 12, no. 3, p. 315–328, doi:10.1016/0191-8141(90)90016-R.

Strahler, A.N., 1950, Davis' concepts of slope development viewed in the light of recent quantitative investigations: Annals of the Association of American Geographers, v. 40, no. 3, p. 209–213, doi:10.1080/00045605009352069.

Tucker, G.E., and Whipple, K.X., 2002, Topographic outcomes predicted by stream erosion models: Sensitivity analysis and intermodel comparison: Journal of Geophysical Research–Solid Earth, v. 107, no. B9, p. 2179, doi:10.1029/2001JB000162.

von Blanckenburg, F., 2005, The control mechanisms of erosion and weathering at basin scale from cosmogenic nuclides in river sediment: Earth and Planetary Science Letters, v. 237, no. 3–4, p. 462–479, doi:10.1016/j.epsl.2005.06.030.

Whipple, K.X., and Tucker, G.E., 1999, Dynamics of the stream-power river incision model: Implications for height limits of mountain ranges, landscape response timescales, and research needs: Journal of Geophysical Research–Solid Earth, v. 104, no. B8, p. 17,661–17,674, doi:10.1029/1999JB900120.

Whittaker, A.C., 2012, How do landscapes record tectonics and climate?: Lithosphere, v. 4, no. 2, p. 160–164, doi:10.1130/RF.L003.1.

Whittaker, A.C., and Boulton, S.J., 2012, Tectonic and climatic controls on knickpoint retreat rates and landscape response times: Journal of Geophysical Research–Earth Surface, v. 117, p. F02024, doi:10.1029/2011JF002157.

Whittaker, A.C., Attal, M., Cowie, P.A., Tucker, G.E., and Roberts, G., 2008, Decoding temporal and spatial patterns of fault uplift using transient river long profiles: Geomorphology, v. 100, no. 3–4, p. 506–526, doi:10.1016/j.geomorph.2008.01.018.

Willenbring, J.K., Codilean, A.T., and McElroy, B., 2013, Earth is (mostly) flat: Apportionment of the flux of continental sediment over millennial time scales: Geology, v. 41, no. 3, p. 343–346, doi:10.1130/G33918.1.

Willett, S.D., and Brandon, M.T., 2002, On steady states in mountain belts: Geology, v. 30, no. 2, p. 175–178, doi:10.1130/0091-7613(2002)030<0175:OSSIMB>2.0.CO;2.

Wobus, C., Hodges, K.V., and Whipple, K.X., 2003, Has focused denudation sustained active thrusting at the Himalayan topographic front?: Geology, v. 31, no. 10, p. 861–864, doi:10.1130/G19730.1.

Wobus, C., Whipple, K.X., Kirby, E., Snyder, N., Johnson, J., Spyropolou, K., Crosby, B., and Sheehan, D., 2006, Tectonics from topography: Procedures, promise, and pitfalls, *in* Willett, S.D., Hovius, N., Brandon, M.T., and Fisher, D.M., eds., Tectonics, Climate, and Landscape Evolution: Geological Society of America Special Paper 398, p. 55–74.

Yanites, B.J., Tucker, G.E., and Anderson, R.S., 2009, Numerical and analytical models of cosmogenic radionuclide dynamics in landslide-dominated drainage basins: Journal of Geophysical Research–Earth Surface, v. 114, p. F01007, doi:10.1029/2008JF001088.

York, D., Evensen, N.M., Martinez, M.L., and Delgado, J.D., 2004, Unified equations for the slope, intercept, and standard errors of the best straight line: American Journal of Physics, v. 72, no. 3, p. 367–375, doi:10.1119/1.1632486.

Science Editor: Christian Koeberl
Associate Editor: Karl W. Wegmann

Manuscript Received 30 June 2015
Revised Manuscript Received 2 May 2016
Manuscript Accepted 5 December 2016

Printed in the USA